

PREDICTIONS OF ION PRODUCTION RATES AND ION NUMBER DENSITIES WITHIN THE DIAMAGNETIC CAVITY OF COMET 67P/CHURYUMOV–GERASIMENKO AT PERIHELION

E. VIGREN AND M. GALAND

Department of Physics, Imperial College London, London SW7 2AZ, UK; e.vigren@imperial.ac.uk

Received 2013 March 7; accepted 2013 May 27; published 2013 July 2

ABSTRACT

We present a one-dimensional ion chemistry model of the diamagnetic cavity of comet 67P/Churyumov–Gerasimenko, the target comet for the ESA *Rosetta* mission. We solve the continuity equations for ionospheric species and predict number densities of electrons and selected ions considering only gas-phase reactions. We apply the model to the subsolar direction and consider conditions expected to be encountered by *Rosetta* at perihelion (1.29 AU) in 2015 August. Our default simulation predicts a maximum electron number density of $\sim 8 \times 10^4 \text{ cm}^{-3}$ near the surface of the comet, while the electron number densities for cometocentric distances $r > 10 \text{ km}$ are approximately proportional to $1/r^{1.23}$ assuming that the electron temperature is equal to the neutral temperature. We show that even a small mixing ratio ($\sim 0.3\%$ – 1%) of molecules having higher proton affinity than water is sufficient for the proton transfer from H_3O^+ to occur so readily that other ions than H_3O^+ , such as NH_4^+ or CH_3OH_2^+ , become dominant in terms of volume mixing ratio in part of, if not throughout, the diamagnetic cavity. Finally, we test how the predicted electron and ion densities are influenced by changes of model input parameters, including the neutral background, the impinging EUV solar spectrum, the solar zenith angle, the cross sections for photo- and electron-impact processes, the electron temperature profile, and the temperature dependence of ion–neutral reactions.

Key words: comets: individual (67P/Churyumov–Gerasimenko) – molecular processes

1. INTRODUCTION

With *Rosetta*, launched 19 yr after *Giotto*, ESA is heading back to a comet, closer than any other cometary mission (Schulz 2009). While most of the previous cometary missions were flybys, taking snapshots at large distances from 21P/Giacobini–Zinner, 1P/Halley, 26P/Grigg–Skjellerup, and 19P/Borelly, *Rosetta* will uniquely follow 67P/Churyumov–Gerasimenko (hereafter referred as 67P/CG) as it approaches the Sun and starts to develop its coma (Schulz 2009). When it reaches perihelion at $\sim 1.3 \text{ AU}$ in 2015 August, the comet is expected to have an outgassing rate of $Q = (4\text{--}8) \times 10^{27} \text{ molecules s}^{-1}$ (Hanner et al. 1985; Benna & Mahaffy 2006; Hansen et al. 2007; Lamy et al. 2007; Tennishev et al. 2008) and to possess a well-developed ionosphere, which will be probed in situ by instruments on the *Rosetta* orbiter down to cometocentric distances of 5–20 km.

67P/CG is a short-period Jupiter family comet first detected in 1969 (Churyumov & Gerasimenko 1972) with an effective radius of $\sim 1.72 \text{ km}$ and a rotational period of 12.4–12.7 hr (Lamy et al. 2007). The orbital period of 67P/CG and its perihelion distance changed from 9.0 yr and 2.7 AU to its present values of $\sim 6.5 \text{ yr}$ and $\sim 1.3 \text{ AU}$, respectively, following a close approach to Jupiter in 1959 (e.g., Hanner et al. 1985; Królikowska 2003). The decrease of the perihelion distance is anticipated to have removed any surface dust mantle that might have acted as a thermal insulator, thereby increasing the activity of the comet (Tennishev et al. 2008). 67P/CG may contain pristine material from its formation phase, and the future investigations of the comet by the instruments on the *Rosetta* orbiter and the lander, *Philae*, can potentially, for example, (1) provide invaluable information on conditions prevailing in the early solar system and (2) teach us more about the link between the chemistry of comets and the chemistry of the collapsing molecular cloud that pre-dated the solar system (Schulz 2009). Regarding the first point, an interesting finding

from the NASA *Stardust* sample return mission to comet Wild 2 was the discovery of minerals requiring high temperatures to form, which indicated the presence of large-scale radial mixing in the protoplanetary disk (e.g., Zolensky et al. 2006). The *Rosetta* mission is of great interest within an astrobiological context, as it is foreseen to provide further clues on whether the late heavy bombardment of comets may have served as a vital deliverer of pre-biotic molecules (and water) to the Earth, thereby possibly contributing to the origin and/or the early evolution of life on our planet (see, e.g., Schulz 2009; Ehrenfreund et al. 2002, and references therein).

To date the evolution of the broader cometary plasma and magnetic environment during the approach toward the Sun has been studied theoretically using MHD or hybrid models (e.g., Wegmann et al. 1987, 1996; Cravens 1989; Huebner et al. 1989; Gombosi 1991; Schmidt et al. 1993; Benna & Mahaffy 2006; Hansen et al. 2007). From these studies, as well as in situ and remote observations of comets, a basic understanding of their structure and plasma environments has arisen, as highlighted in the reviews by Cravens (1987), Ip (2004), Cravens & Gombosi (2004), and Ma et al. (2008). The magnetized plasma controlled by the solar wind is separated from the plasma of cometary origin by a transition region. Within this region, referred to as the *contact surface*, the inward-pointing magnetic pressure gradient force is balanced by the outward-pointing ion–neutral drag force (see, e.g., Cravens 1989, and references therein). Its location is strongly influenced by both the solar wind and ionospheric conditions. The *Giotto* flyby of comet 1P/Halley (heliocentric distance of $\sim 0.9 \text{ AU}$) revealed a contact surface about 4000–4500 km from the nucleus (Neubauer et al. 1986). Comet 26P/Grigg–Skjellerup was visited by *Giotto* in 1992 at a heliocentric distance of about 1 AU and was found to have an outgassing rate of $\sim 7.2 \times 10^{27} \text{ s}^{-1}$. The closest approach of $\sim 120 \text{ km}$ was identified as being outside the contact surface, estimated at $\sim 82 \text{ km}$ by Flammer & Mendis (1993). As for 67P/CG, Hansen et al. (2007) and Benna & Mahaffy

(2006) predict the contact surface to be located at ~ 30 km (~ 70 km on the nightside) from the nucleus at perihelion. The actual location—expected to be highly variable with solar conditions—will be determined through measurements by the Flux Gate Magnetometer (MAG; Glassmeier 2007) on board the *Rosetta* orbiter. The development of a sensible ionospheric model is critical to interpret the location of the contact surface of 67P/CG and its variability.

Inward of the contact surface, the so-called *diamagnetic cavity* is a magnetic field free environment, mostly shielded from the solar wind, with ionization rates expected to be dictated primarily by solar EUV photons, suprathermal photoelectrons, and their associated secondary (tertiary, etc.) electrons ejected in electron-impact ionization events. The chemistry of 67P/CG is planned to be probed both on the surface and in the gas phase (Schulz 2009). In the gas phase, molecules can be synthesized through chemical reaction networks involving, e.g., ion–neutral, radical–radical, and ion–electron (dissociative recombination) reactions. To combine in situ observations with chemical modeling will be critical to distinguish such synthesized *daughter molecules*, from the *parent molecules*, which are sublimated directly from the cometary surface.

Most studies on cometary ionospheres have so far been focusing mainly on 1P/Halley, which was visited by the *Giotto* spacecraft in 1986 March (e.g., Cravens & Körözmezey 1986; Cravens et al. 1987; Cravens 1989; Körözmezey et al. 1987; Wegmann et al. 1987; Bhardwaj et al. 1990; Häberli et al. 1996; Haider & Bhardwaj 1997, 2005; Lovell et al. 2004; Rubin et al. 2009). Following the perihelion passage of the very active long-period comet C/1995 Hale–Bopp in 1997, efforts (e.g., Rodgers & Charnley 2001) were undertaken to reproduce in chemical models the molecular abundances inferred from remote-sensing observations (e.g., Bockelée-Morvan et al. 2000). Both Halley and Hale–Bopp are, however, at perihelion significantly more outgassing comets than 67P/CG, due to different surface characteristics and their larger nucleus sizes. In 1985 September, the *International Cometary Explorer* spacecraft visited 21P/Giacobini–Zinner, which is of size similar to that of 67P/CG. At closest approach the spacecraft was about 7800 km from the nucleus, with H_2O^+ being significantly more abundant than H_3O^+ in this almost collision-free region (Ogilvie et al. 1986). In terms of outgassing rate comet 19P/Borelly is in between Halley and 67P/CG for similar heliocentric distances. The ion chemistry of this comet was probed by the ion mass spectrometer on board the *Deep Space 1* spacecraft in 2001 September (heliocentric distance of 1.36 AU), but only for cometocentric distances exceeding 2200 km, where simple ions, such as OH^+ and H_2O^+ , were found to dominate in terms of volume mixing ratio (Nordholt et al. 2003).

Only a few studies have been dedicated to the deep ionospheres of low outgassing comets, including 67P/CG. Bhardwaj (2003) did a comparative study of the photoionization rates and electron-impact ionization rates for comets with different outgassing rates at 1 AU and found that at a given cometocentric distance the relative importance of electron-impact ionization increases with the outgassing rate. They found also that the photoionization rate for low outgassing comets with $Q = 1 \times 10^{28} \text{ s}^{-1}$ and below (including comets such as 67P/CG) increases with decreased cometocentric distance all the way to the surface. For comets, such as 1P/Halley, with higher outgassing rates ($Q = 7 \times 10^{29} \text{ s}^{-1}$), one photoionization peak was predicted associated with solar EUV deposition, while the strongest outgassing comets (e.g., comets such as C/1995

Hale–Bopp with $Q > 10^{31} \text{ s}^{-1}$) displayed two photoionization peaks, the second peak, at lower cometocentric distances, being associated with soft X-ray deposition. von Oertzen (2003) calculated electron number densities for 67P/CG at different heliocentric distances (different phases of the *Rosetta* mission) predicting peak values (near the cometary surface) of $\sim 10^4$, 10^3 , 10, and $< 10^{-2} \text{ cm}^{-3}$ for heliocentric distances of 1.3 (perihelion), 2.0, 3.0, and 4.0 AU, respectively. Benna & Mahaffy (2006) predicted, however, at perihelion a peak electron number density nearly an order of magnitude higher than von Oertzen (2003).

In the present paper, we solely focus on perihelion and assess the ionization rates and ion number densities as a function of cometocentric distance within the diamagnetic cavity of 67P/CG. The model is driven by input parameters expected for this comet at perihelion (see Section 3). Compared with von Oertzen (2003), who applied an ionization frequency of the H_2O molecule constant with cometocentric distance, we treat the different ionization sources in a more detailed manner and take into account the attenuation of the impinging solar radiation, which becomes significant close to the surface. In contrast to von Oertzen (2003) and Benna & Mahaffy (2006), we also consider in our model other neutral species than H_2O and investigate their effect on the ion chemistry. This allows us to predict the fractional abundance of H_3O^+ to the total ion population as a function of cometocentric distance. Ma et al. (2008) stated that proton transfer from H_3O^+ to molecules with higher proton affinity than H_2O is the most important chemical reaction occurring in the innermost coma of active comets. Ionospheric models of 1P/Halley predict, in fact, that even though the volume-mixing ratio of ammonia (NH_3) is low (typically less than a few percent), the NH_4^+ ion becomes more abundant than the hydronium ion, H_3O^+ , at low cometocentric distances due to the rapid proton transfer from H_3O^+ (and other protonated molecules) to NH_3 (e.g., Ip, 1989; Haider & Bhardwaj 1997, 2005; see also the review by Mendis 1988, and references therein).

The results we propose represent predictions to the anticipated observations by *Rosetta* at perihelion. Comparison of the modeling results will in particular be highly relevant with the in situ *Rosetta* measurements of thermal electron and ion number densities in the diamagnetic cavity of 67P/CG by the Langmuir Probe (LAP; Eriksson et al. 2007), the Mutual Impedance Probe (MIP; Trotignon et al. 2007), the radio science investigations (RSI; Pätzold et al. 2007), and the *Rosetta* Orbiter Spectrometer for Ion and Neutral Analysis (ROSINA; Balsiger et al. 2007). We present the energy deposition and ionospheric models applied to the environment of 67P/CG (Section 2), the physical quantities used as input to drive the models (Section 3), and the calculated production rates and number densities of thermal electrons and selected ions for our baseline simulation (Section 4). In Section 5, we conduct a series of sensitivity tests to show how the model predictions are influenced by changes in different input parameters. Conclusions are given in Section 6.

2. IONOSPHERIC MODEL

2.1. Ion Production Rates due to Photo- and Electron-impact Ionization

The production rate of ion species j due to photoionization at the cometocentric distance r is calculated by numerically

solving the integral

$$P_{j,\text{photo}}(r) = \sum_k n_k(r) \int \sigma_k^j(\lambda) I(\lambda, r) d\lambda, \quad (1)$$

where the sum goes over the neutral species $k = \text{H}_2\text{O}$ and CO , $n_k(r)$ is the number density of k at r , $\sigma_k^j(\lambda)$ is the partial photoionization cross section of k that leads to ion species j at wavelength λ , and $I(\lambda, r)$ is the attenuated spectral irradiance at λ and r . The spectral range extends from 0.1 nm to the ionization thresholds. The energy (or wavelength) resolution of the cross sections is dictated by the resolution of the impinging solar EUV spectrum corresponding to 1 nm (see Section 3.2). $I(\lambda, r)$ is derived from the Beer–Lambert Law:

$$I(\lambda, r) = I(\lambda, r_\infty) \exp[-\tau(\lambda, r)], \quad (2)$$

where $I(\lambda, r_\infty)$ is the spectral irradiance at λ at the top of the cometary coma, where absorption of solar radiation is negligible, here taken as $r_\infty = 1200$ km, and $\tau(\lambda, r)$ is the optical depth at λ and r . For a solar zenith angle (SZA), $\chi < 90^\circ$, the optical depth at r is given by (e.g., Rees 1989)

$$\tau(\lambda, r, \chi) = \sum_k \sigma_k^{\text{abs}}(\lambda) \int_r^{r_\infty} \frac{n_k(r')}{\sqrt{1 - (r/r')^2 \sin^2 \chi}} dr' \quad (3)$$

where $\sigma_k^{\text{abs}}(\lambda)$ is the photoabsorption cross section of neutral species k at wavelength λ . A photoionization process associated with the ionization potential IP, occurring at λ , gives rise to a photoelectron with the energy $E = hc/\lambda - \text{IP}$, where h is Planck's constant and c is the speed of light. In case of a double ionization process we assume that the released electrons share evenly the kinetic energy. From the attenuated solar radiation at r , the ambient neutral number densities, and the considered photoionization processes (their cross sections and threshold energies) we then compute the photoelectron intensity, assumed isotropic, at r .

The production rate of ion species j due to electron-impact ionization is given by

$$P_{j,e\text{-impact}}(r) = 2\pi \sum_k n_k(r) \int \int_{\mu=-1}^1 I_e(E, \mu, r) \sigma_{EI,k}^j(E) d\mu dE, \quad (4)$$

where the sum is over neutral species k , $\sigma_{EI,k}^j(E)$ is the partial electron-impact ionization cross section of k that leads to ion species j at the electron energy E , and $I_e(E, \mu, r)$ is the suprathermal electron intensity at E , r , and μ , the latter parameter which is defined by $\mu = \cos \theta$, where θ is the inclination angle between the trajectory of the impinging suprathermal electron and the local vertical. The integral over E is evaluated from the ionization threshold to the maximum energy of the photoelectrons.

The suprathermal electron intensity $I_e(E, \mu, r)$ is calculated by solving the Boltzmann equation assuming steady-state conditions (Rees 1989). The profiles of the photoelectron spectrum and the number densities of H_2O and CO are used as input into this calculation together with the cross sections and excitation/ionization energies for electron impact processes on H_2O and CO . In this study, we have adapted to the environment of 67P/CG an electron transport model of Titan's ionosphere (see Galand et al. 2006, 2010). The electron-impact cross-section set used is discussed in detail in Section 3.4. The energy distribution

function of secondary electrons ejected in the electron-impact ionization of H_2O (and CO), as a function of the incident electron energy, has been adopted from Opal et al. (1971). (In the case of double ionization events, we let for simplicity one of the ejected electrons obtain an energy of 0 eV.) Examples of photoelectron source functions calculated from the Beer–Lambert Law and suprathermal electron mean intensities derived from the Boltzmann equation are provided in the Appendix.

The electron production rate due to photoionization, $P_{e,\text{photo}}(r)$, and that due to electron impact ionization, $P_{e,e\text{-impact}}(r)$, are obtained by summing over all j the $P_{j,\text{photo}}(r)$ and $P_{j,e\text{-impact}}(r)$ values, respectively (multiplying each term by the charge state of j). It is noted that the total production rates of the multiply charged species CO^{2+} , O^{2+} , and C^{2+} are about four orders of magnitude smaller than the total electron production rate. Therefore, we neglect these multiply charged species in our chemical modeling.

2.2. Prediction of Ion Number Densities

The continuity equation for ion species j at r is given by

$$\frac{\partial n_j(r, t)}{\partial t} + \nabla \cdot (n_j(r, t) \mathbf{u}_j(r)) = P_j(r, t) - L_j(r, t) n_j(r, t), \quad (5)$$

where each term represents a rate of change of the number density of ion species j per time. The second term on the left-hand side represents the flux divergence with $\mathbf{u}_j(r)$ being the drift velocity of j at r . On the right-hand side of Equation (5) $P_j(r, t)$ and $L_j(r, t)$ are the production and loss rates of j at cometocentric distance r and time t , with the units of $\text{cm}^{-3}\text{s}^{-1}$ and s^{-1} , respectively. The time dependencies of n_j , P_j , and L_j are included for solving numerically the equation, while the ion densities presented in Sections 4 and 5 are the solutions after convergence was reached.

The ion species are assumed transported in a radial direction by the neutral gas, and the flux divergence term of Equation (5) can therefore be reduced to

$$\nabla \cdot (n_j(r, t) \mathbf{u}_j(r)) = \frac{1}{r^2} \frac{\partial}{\partial r} (r^2 n_j(r, t) u(r)), \quad (6)$$

where $u(r)$ is taken to be equal to the radial speed, $u_w(r)$, of the H_2O molecules at r (see Figure 1(b)).

The value of $P_j(r, t)$ is given by

$$P_j(r, t) = P_{j,\text{photo}}(r) + P_{j,e\text{-impact}}(r) + P_{j,\text{chem}}(r, t), \quad (7)$$

where $P_{j,\text{photo}}(r)$ and $P_{j,e\text{-impact}}(r)$ are defined in Section 2.1 and where $P_{j,\text{chem}}(r, t)$ is the production rate of j at r and t due to ion–neutral reactions. The selection of ion species and the ion reactions (production and loss) considered in the model (two- and three-body ion neutral reactions, as well as dissociative recombination reactions) are presented in Sections 3.6 and 3.7.

The cometary coma is divided into spherical shells s_1, s_2, \dots , wherein all the input parameters such as neutral densities and ionization rates are assumed to be constant. In the innermost shell, s_1 , there is no ion inflow from below. A set of initial ion number densities (close to zero) is assumed, and the chemical evolution in s_1 is assessed by solving the set of coupled continuity equations in a numerical manner using time steps of 0.05 s. For s_i with $i > 1$, ion densities are retrieved in a similar way, but the ion inflow from s_{i-1} is taken into account and the *initial* number density of j is set equal to the number density of j determined in s_{i-1} . The thermal electron number density is

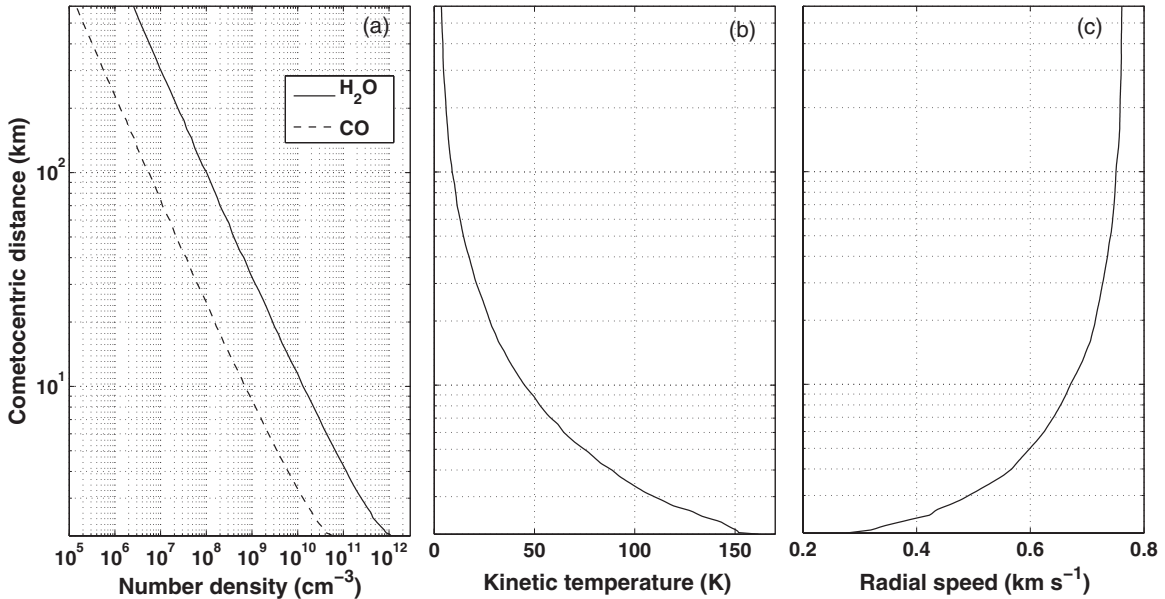


Figure 1. (a) Number densities of H₂O (solid) and CO (dashed), (b) kinetic temperature of H₂O, and (c) radial speed of H₂O, vs. cometocentric distance (data from Tenishev et al. 2008). For our baseline simulation, we set the electron temperature equal to the kinetic temperature of H₂O, shown in panel (b), and the ion radial speed to the radial speed of H₂O, shown in panel (c).

derived from the ion number densities assuming charge balance. The ion number densities (and therefore the electron number density) converge rapidly at all r , the time required (less than 10 minutes) being significantly smaller than the rotational period of 67P/CG (12.4–12.7 hr as derived by Lamy et al. 2007). The following criterion

$$|\partial n_j / \partial t| < 0.01 \times \min\{P_j, L_j n_j, |\nabla \cdot (n_j \mathbf{u}_j)\}\} \quad (8)$$

is fulfilled for all ion species in s_i after 8–9 minutes overall, and after less than a minute for $r < 500$ km.

3. INPUT PARAMETERS

3.1. Neutral Background in the Model

We use as input into our model of 67P/CG the number densities of H₂O and CO, the kinetic temperature, $T_w(r)$, of H₂O, and the radial speeds, $u_w(r)$, of H₂O, versus cometocentric distance, r , derived from the kinetic model of Tenishev et al. (2008) at perihelion along the subsolar direction (SZA = 0°). These authors used a newly developed direct simulation Monte Carlo method in which components of the coma are coupled through momentum exchange and photochemical processes. The surface conditions (the temperature and water outward flux) assumed are based on a model by Davidsson & Gutiérrez (2004, 2005, 2006). All neutral data used in our simulations are shown in Figure 1. It is noted that in particular for $r > 10$ km the number densities are roughly in proportion to $1/r^2$. The $n(\text{CO})/n(\text{H}_2\text{O})$ ratio is within 0.05–0.06 for all r . The kinetic temperature and radial speeds for CO are largely similar (within a few percent) to the values for H₂O in the model by Tenishev et al. (2008), and we consider $T = T_w$ and $u = u_w$ for all species in our model.

Besides H₂O and CO, the carbon dioxide molecule CO₂ is typically observed as the third most abundant molecule within the coma of active comets near perihelion (see, e.g., Ehrenfreund & Charnley 2000). Its presence, at a mixing ratio of a few percent, would only slightly alter the calculated electron production rate profile. The proton affinity for CO₂ is lower than for H₂O, such that no proton transfer occurs from the

abundant H₃O⁺ ion to CO₂. Moreover, the main ion formed in the photoionization and electron impact ionization of CO₂ is the CO₂⁺ ion, which is reactive by electron transfer with H₂O, and therefore it is readily lost to form H₂O⁺ and to return CO₂ (the 300 K rate coefficient reported by Karpas et al. 1978 for this reaction is $2.04 \times 10^{-9} \text{ cm}^3 \text{ s}^{-1}$). Thus, we anticipate that the inclusion of CO₂ would not severely affect the big picture of the ion chemistry within the diamagnetic cavity of 67P/CG, and we therefore ignore it in the present study.

3.2. Solar EUV Spectrum

The incident solar EUV spectrum used in our “baseline simulation” is shown in Figure 2(a). It is based on measurements by the Thermosphere Ionosphere Mesosphere Energetics and Dynamics (TIMED)/Solar EUV Experiment (SEE; Woods et al. 2005). We use the spectrum measured on 2005 January 2 (decreasing solar activity phase with $F_{10.7} = 100 \times 10^{22} \text{ W m}^{-2} \text{ Hz}^{-1}$) extrapolated to a distance of 1.29 AU and corresponding to conditions expected to be experienced by *Rosetta* in 2015 August. The ionization thresholds for H₂O and CO are at 98.3 and 88.5 nm, respectively (Avakyan et al. 1998), so there is no need to consider the solar flux at wavelengths longward of 100 nm. The strongest feature seen in the EUV spectrum is the solar He II line at 30.4 nm. In Figure 2(b), we show the spectral irradiance ratio of the EUV radiation between extreme conditions (solar maximum and solar minimum) and the default case shown in Figure 2(a). The largest discrepancies are seen toward short wavelengths (soft X-rays), and a pronounced variability is also seen in the 33–34 nm bin, associated with the hot coronal Fe XVI line at 33.5 nm (see, e.g., Woods & Eparvier 2006).

3.3. Cross Sections for Photo-processes

The total H₂O photoabsorption cross section and partial H₂O photoionization cross sections yielding the production of H₂O⁺ (IP = 12.62 eV), OH⁺ (IP = 18.12 eV), H⁺ (IP = 16.95 eV), and O⁺ (IP = 19.00 eV) are shown versus wavelength in Figure 3(a). The data are based on Schunk & Nagy (2009), Avakyan et al.

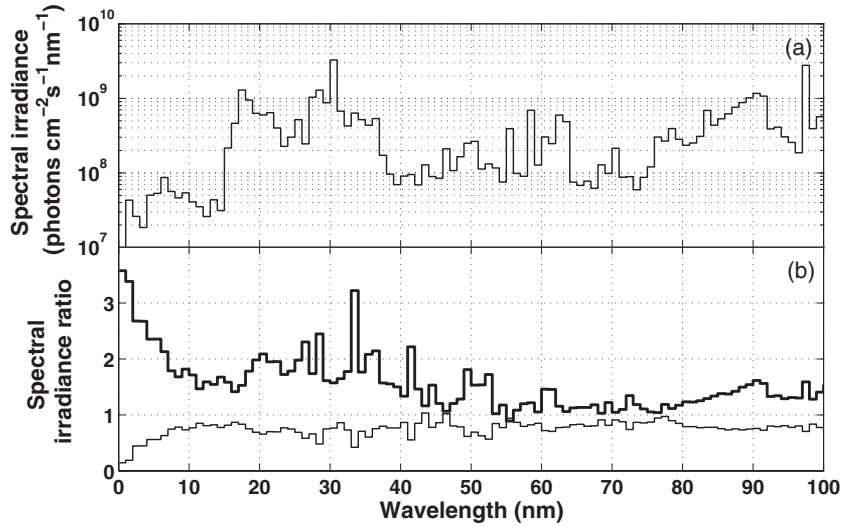


Figure 2. (a) Incident spectral irradiance used by default in our runs. (b) Spectral irradiance, relative to the spectrum in panel (a), for solar maximum (bold) and solar minimum conditions. All spectra were derived from TIMED/SEE measurements and extrapolated in distance to 1.29 AU. The dates for the measurements were 2005 January 2 (standard, $F_{10,7} = 100 \times 10^{22} \text{ Wm}^{-2} \text{ Hz}^{-1}$), 2002 February 9 (solar maximum, $F_{10,7} = 174 \times 10^{22} \text{ Wm}^{-2} \text{ Hz}^{-1}$) and 2008 January 20 (solar minimum, $F_{10,7} = 70 \times 10^{22} \text{ Wm}^{-2} \text{ Hz}^{-1}$).

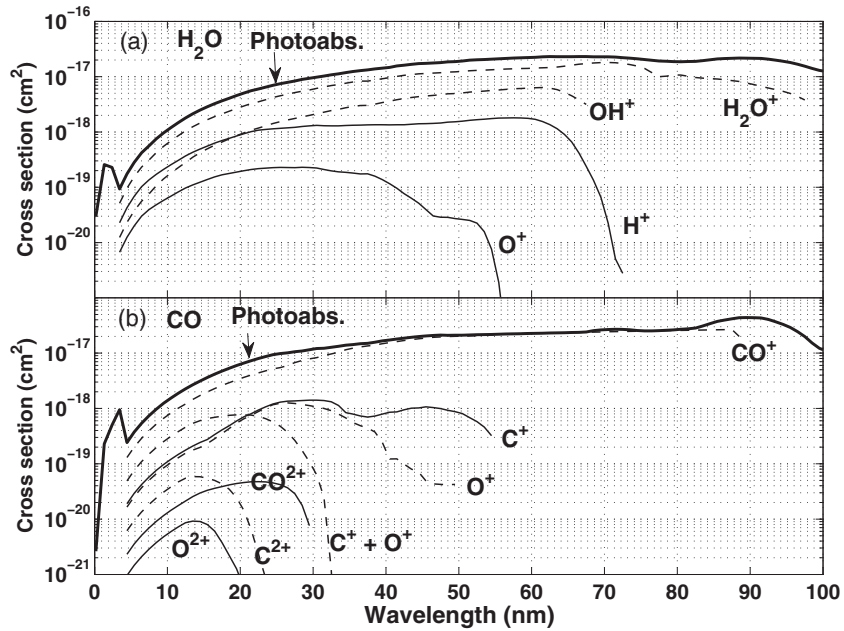


Figure 3. Cross sections used for photo-processes of (a) H₂O and (b) CO. The structures in the photoabsorption cross section at low wavelengths are due to core ionization.

(1998), and Chan et al. (1993a). The total CO photoabsorption cross section and the partial CO photoionization cross sections for the production of CO⁺, O⁺ (IP = 24.65 eV), C⁺ (IP = 22.37 eV), C⁺ + O⁺ (IP = 35.98 eV), CO²⁺ (IP = 41.25 eV), C²⁺ (IP = 45.75 eV), and O²⁺ (59.87 eV) are shown versus wavelength in Figure 3(b). In the figure, for clarity purposes, we show the total ionization cross section for the production of CO⁺, while in the model we include cross sections for the production of CO⁺ in the ground electronic state $X^2\Sigma^+$ (IP = 14.00 eV) and the two first electronically excited states (IP = 16.50 eV and 19.70 eV). The data set shown in Figure 3(b) is based on Chan et al. (1993b), Masuoka & Nakamura (1993), Masuoka & Samson (1981), Plummer et al. (1977), and Avakyan et al. (1998).

Both the H₂O and CO photoabsorption cross sections display a peak structure at about 2–5 nm, which is due to core ionization

(mainly leading to multiple ionization due to Auger decay). The solar irradiance is, however, very small at these wavelengths (see Figure 2(a)). Photons with absorption cross section of $<10^{-18} \text{ cm}^2$ are in addition expected to be absorbed mainly where the column density in the line of sight toward the Sun is $>10^{18} \text{ cm}^2$, which is larger than the column density from the surface of the comet equal to $\sim 1 \times 10^{17} \text{ cm}^2$. Therefore, for simplicity, we keep the branching fractions for the different ionization channels fixed below 5 nm and scale the partial ionization cross sections to the total absorption cross section.

3.4. Cross Section for Electron Impact Processes

The cross sections used for different electron scattering processes on H₂O and CO as a function of energy are shown in Figure 4. It is noted that for electron energies below about

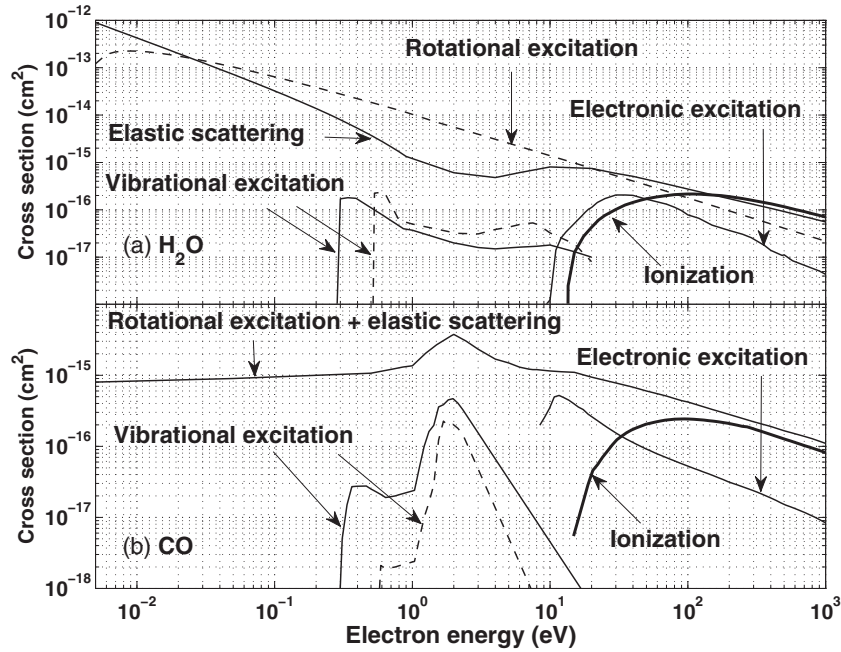


Figure 4. Cross sections used in the model for electron-impact processes on (a) H_2O and (b) CO . For the vibrational excitations of H_2O the solid line is for the excitation of stretching modes and the dashed line is for the excitation of the bending mode. For the vibrational excitations of CO the solid line is for the $v = 0 \rightarrow 1$ transition and the dashed line is for the $v = 0 \rightarrow 2$ transition.

12.62 eV (the ionization threshold of H_2O) the cross sections for the scattering processes do not influence the calculated ionization rates. They are, however, appropriate to display as they influence the cooling rate of suprathermal electrons, and therefore useful as argument for the selection of our electron temperature profile (see Section 3.5).

Only the total ionization cross sections are shown for visibility, but in the model individual ionization processes are included (see Section 3.4.1). For CO we consider excitation into specific electronic states, though in Figure 4(b) we only show the total cross section for electronic excitation. Due to limited energy resolution, experimentally derived cross sections for electron-impact elastic scattering are often not for pure elastic scattering, but rather for rotational excitation and pure elastic scattering combined. For H_2O we have separated pure elastic scattering from rotational excitation as described in Section 3.4.4, while for CO we use the cross section for the processes combined and neglect the small electron energy loss (of a few meV) associated with the rotational excitations.

3.4.1. Ionization Cross Section

The electron impact ionization cross sections of H_2O are taken from Itikawa & Mason (2005). Cross sections are given for the production of H_2O^+ , OH^+ , O^+ , O^{2+} , H_2^+ , and H^+ . The energy required for the formation of H_2^+ and O^{2+} is 20.70 eV and 54.10 eV, respectively.

The electron-impact ionization cross sections of CO for the production of CO^+ , $\text{C}^+ + \text{O}$, $\text{O}^+ + \text{C}$, and CO^{2+} are taken from Mangan et al (2000). The electron impact ionization cross sections for the production of $\text{C}^+ + \text{O}^+$, $\text{C}^{2+} + \text{O}$, and $\text{C} + \text{O}^{2+}$ are taken from Tian & Vidal (1999).

3.4.2. Electronic Excitation

The cross sections for individual electronic excitation processes derived experimentally and theoretically for H_2O display large (nearly an order of magnitude) discrepancies (see Thorn

2008). Therefore, instead of treating the electronic excitation processes individually we focus on the total cross section for electronic excitation. We use the total scattering cross section, $\sigma_{\text{total}}(E)$, and ionization cross section from Itikawa & Mason (2005). For energies above 7.5 eV we use the $\sigma_{EE, \text{ioni}}(E)/\sigma_{\text{total}}(E)$ ratios recommended by Muñoz et al. (2007) where $\sigma_{EE, \text{ioni}}$ denotes the combined cross section for electronic excitations and ionizations. From the computed $\sigma_{EE, \text{ioni}}(E)$ values we then subtract the $\sigma_{\text{ioni}}(E)$ values used. This gives us an estimate of $\sigma_{EE}(E)$ as shown in Figure 4(a). The value is significantly higher than the one obtained by summing the cross sections for the excitations into individual electronic states as derived by Thorn (2008). For this reason we show in Sections 4.1 and 5.5 how sensitive the predicted ionization rates and electron number densities are to a decreased energy-dependent electron-impact electronic excitation cross section of H_2O . For the electronic excitations at energies above the ionization threshold of H_2O we adopt an average electron energy loss of $W_{EE} = 10$ eV based on Anzai et al. (2012) and the excitation energies listed by Thorn (2008) for individual electronic states of the water molecule.

For CO we consider excitation from the electronic ground state ($X^1\Sigma^+$) to nine different electronically excited states. For the excitation into $a'^3\Sigma^+$ (excitation energy of 6.863 eV), $c^3\Pi$ (11.416 eV), $d^3\Delta$ (7.516 eV), $j^3\Sigma^+$ (11.265 eV), and $D^1\Delta$ (8.108 eV), the cross sections were calculated based on Jackman et al. (1977). For the excitation into $b^3\Sigma^+$ (10.394 eV), $a^3\Pi$ (6.01 eV), and $I^1\Sigma^-$ (8.003 eV) the cross sections were taken (and extrapolated) from Brunger & Buckman (2002). Finally, for the excitation into $A^1\Pi$ (8.028 eV) the cross sections were taken from Kato et al. (2007, the BEf-scaling approach). The listed excitation energies are all taken from Brunger & Buckman (2002).

3.4.3. Vibrational Excitation

The cross sections for the excitation of the symmetric and anti-symmetric stretching modes of H_2O are combined and

taken from Itikawa & Mason (2005). The cross section for excitation of the bending mode is taken from the same work. The energy required for the excitation of the stretching modes (bending mode) is approximately 0.453 eV (0.198 eV). We consider here only the lowest vibrational excitations of H₂O molecules starting in their vibrational ground state.

The vibrational excitation cross sections $v = 0 \rightarrow 1$ and $v = 0 \rightarrow 2$ for CO are taken from Poparic et al. (2006). For energies approaching the threshold of the $v = 0 \rightarrow 1$ transition we have taken values from Brunger & Buckman (2002). The excitation energies for $v = 0 \rightarrow 1$ and $v = 0 \rightarrow 2$ are ~ 0.27 and 0.54 eV, respectively.

3.4.4. Rotational Excitation and Elastic Scattering

The cross sections for the electron-impact elastic scattering of CO were taken from Brunger & Buckman (2002). These cross sections include rotational excitation. For energies below 1 eV the cross sections displayed in Figure 4(b) are based on values of the grand total scattering cross section of CO, also taken from Brunger & Buckman (2002).

For the rotational excitation of H₂O we take the cross sections from Muñoz et al. (2007) where energies range from 1 eV to 10 keV. The cross sections were calculated for an assumed rotational temperature of 300 K. However, the cross sections at 1, 1.5, 2, 3, 4, and 5 eV are only about 5% higher than the values listed in Itikawa & Mason (2005) for the cross section of the $J = 0-1$ rotational transition. For energies below 1 eV we display in Figure 4(a) the cross sections listed for the $J = 0-1$ rotational transition in Itikawa & Mason (2005). We assume an average energy loss of $W_{\text{rot}} = 4$ meV for the electrons in the rotational excitation processes (see, e.g., Muñoz et al. 2007).

The agreement between the total-scattering cross sections derived theoretically and experimentally by Muñoz et al. (2007) improves with increasing energy. We use the pure elastic cross sections calculated by Muñoz et al. (2007) for $E > 30$ eV. For $E \leq 30$ eV we use cross sections for vibrationally elastic scattering from Itikawa & Mason (2005), and from these values we subtract the cross sections for rotational excitation. For $E < 1$ eV we show in Figure 4(a) the cross sections provided for $J = 0 \rightarrow 0$ in Itikawa & Mason (2005).

3.5. Electron Temperature Profile

The thermal electron temperature, T_e , is a fundamental parameter in ionospheric model calculations, as it affects the dissociative recombination loss rate of free electrons with molecular ions. The efficiency of the dissociative recombination process increases in general with reduced electron temperature, with rate coefficients at $T_e = 10$ K being up to 50 times higher than at $T_e = 1000$ K. In an environment controlled by photochemical equilibrium and with a specific electron production rate, the electron number density can therefore be increased up to ~ 7 times through the increase of T_e from 10 to 1000 K.

We assume in our baseline simulation that the thermal electron temperature, T_e , is equal to the kinetic temperature of H₂O as shown in Figure 1(b). Due to the polar nature of the water molecule it is a very efficient coolant for electrons (see, e.g., Cravens & Körözmezey 1986). In particular for $r < 100$ km where the H₂O number densities are expected to exceed 10^8 cm⁻³ (see Figure 1(a)), the high electron-impact rotational excitation cross sections at sub-eV energies (see Figure 4(a)) are anticipated to cause a rapid energy degradation of suprathermal electrons. The model calculations for comet 1P/Halley at

~ 1 AU by Körözmezey et al. (1987), Gan & Cravens (1990), and Ip (1985) all showed that the electron temperature should be similar to the neutral temperature within at least 1000 km from the nucleus, where for 1P/Halley at ~ 1 AU, the H₂O number densities exceed 10^8 cm⁻³. The assumption that $T_e = T_n$ may not hold throughout the diamagnetic cavity of 67P/CG. We have not here assessed the contributions of heating processes of the thermal electron population on the thermal electron temperature (this is a subject of a future study). Therefore, in Section 5.6 the sensitivity on the predicted electron number densities of using elevated electron temperatures is assessed.

3.6. Ion–Neutral Reactions Considered in the Model

3.6.1. Ion–Neutral Reactions and Their Temperature Dependence

The dominant primary ions from the ionization of H₂O are H₂O⁺, OH⁺, H⁺, O⁺, and H₂⁺, while those from the ionization of CO are CO⁺, C⁺, and O⁺. All of these ions are reactive with H₂O and some of them with CO. Rate coefficients for these ion–neutral reactions have been determined experimentally at least at room temperature. In their reaction list, provided for astrochemical modeling, Woodall et al. (2007) suggest a $(T/300)^{-0.5}$ dependence for all exoergic ion–neutral reactions involving neutrals with a dipole moment in the excess of 0.9 D. We adopt therefore a temperature dependence of $(T/300)^{-0.5}$ for ion–neutral reactions involving H₂O (dipole moment of 1.85 D) as the neutral reactant. We set no temperature dependence for the ion–neutral reactions involving CO as its dipole moment is ~ 0.12 D. In Table 1, we list the rate coefficients determined at 300 K for the ion–neutral reactions between the dominant primary ions and the major neutral species H₂O and CO (IN1–IN14 in Table 1). The primary ions react with H₂O or CO yielding primary ions or two new ion species, H₃O⁺ or HCO⁺. It is noted that HCO⁺ are produced through five of the reactions listed in Table 1. The HCO⁺ ion is not reactive with CO but reacts with H₂O to form H₃O⁺ + CO (IN15 of Table 1). The hydronium ion, H₃O⁺, is a closed shell ion, which is not reactive with H₂O or CO. Should we not consider other neutral constituents (or three-body reactions) it would be a so-called terminal ion in our model, which chemically would be lost only through dissociative recombination with free thermal electrons (see Section 3.7). We introduce to the chemistry also molecules, M_{HPA}, with higher proton affinity than H₂O, at a volume mixing ratio of 1% that reacts with H₃O⁺ to form M_{HPA}H⁺ with a 300 K rate coefficient according to IN16 in Table 1 and with a rate coefficient proportional to $(T/300)^{-0.5}$ (see Section 3.6.2). Finally, we include also three-body reactions (see IN17 and IN18 of Table 1) forming cluster ions, M⁺_{CLUS}, with three-body rate coefficients proportional to $(T/300)^{-4.0}$ (see Section 3.6.3).

It is noted that most of the earlier studies on cometary ionospheres do not seem to consider the possible temperature dependencies of ion–neutral reactions (e.g., Haider & Bhardwaj 2005; Rubin et al. 2009). The impact on the calculated ion (and electron) number densities of removing the temperature dependencies of all ion–neutral reactions is assessed in Section 4.3.

3.6.2. Loss of H₃O⁺ through Reactions with Molecules with Higher Proton Affinity Than H₂O

Observations of comets have shown that molecules such as CH₃OH, NH₃, HCN, H₂S, HCOOH, CH₃CN, and CH₃CHO are sublimated as parent species from cometary nuclei (and dust particles) at a total rate often exceeding the level of 1%

Table 1
Ion–Neutral (IN) Reactions Considered in the Model

Reaction	Reactants	Products	Rate Coefficient	Reference
IN1	$\text{H}_2\text{O}^+ + \text{H}_2\text{O}$	$\text{H}_3\text{O}^+ + \text{OH}$	2.10×10^{-9}	Huntress & Pinizzotto (1973)
IN2	$\text{H}_2\text{O}^+ + \text{CO}$	$\text{HCO}^+ + \text{OH}$	5.00×10^{-10}	Jones et al. (1981)
IN3	$\text{OH}^+ + \text{H}_2\text{O}$	$\text{H}_2\text{O}^+ + \text{OH}$	1.59×10^{-9}	Huntress & Pinizzotto (1973)
IN4	$\text{OH}^+ + \text{H}_2\text{O}$	$\text{H}_3\text{O}^+ + \text{O}$	1.30×10^{-9}	Huntress & Pinizzotto (1973)
IN5	$\text{OH}^+ + \text{CO}$	$\text{HCO}^+ + \text{O}$	1.05×10^{-9}	Jones et al. (1981)
IN6	$\text{H}^+ + \text{H}_2\text{O}$	$\text{H}_2\text{O}^+ + \text{H}$	6.90×10^{-9}	Smith et al. (1992)
IN7	$\text{CO}^+ + \text{H}_2\text{O}$	$\text{H}_2\text{O}^+ + \text{CO}$	1.72×10^{-9}	Huntress et al. (1980)
IN8	$\text{CO}^+ + \text{H}_2\text{O}$	$\text{HCO}^+ + \text{OH}$	8.84×10^{-10}	Huntress et al. (1980)
IN9	$\text{O}^+ + \text{H}_2\text{O}$	$\text{H}_2\text{O}^+ + \text{O}$	3.20×10^{-9}	Adams et al. (1980)
IN10	$\text{C}^+ + \text{H}_2\text{O}$	$\text{HCO}^+ + \text{H}$	2.70×10^{-9}	Anicich et al. (1976) ^a
IN11	$\text{H}_2^+ + \text{H}_2\text{O}$	$\text{H}_2\text{O}^+ + \text{H}_2$	3.90×10^{-9}	Kim & Huntress (1975)
IN12	$\text{H}_2^+ + \text{H}_2\text{O}$	$\text{H}_3\text{O}^+ + \text{H}$	3.40×10^{-9}	Kim & Huntress (1975)
IN13	$\text{H}_2^+ + \text{CO}$	$\text{HCO}^+ + \text{H}$	2.16×10^{-9}	Kim & Huntress (1975)
IN14	$\text{H}_2^+ + \text{CO}$	$\text{CO}^+ + \text{H}_2$	6.44×10^{-10}	Kim & Huntress (1975)
IN15	$\text{HCO}^+ + \text{H}_2\text{O}$	$\text{H}_3\text{O}^+ + \text{CO}$	2.50×10^{-9}	Adams et al. (1978)
IN16	$\text{H}_3\text{O}^+ + M_{\text{HPA}}$	$M_{\text{HPA}}\text{H}^+ + \text{H}_2\text{O}$	2.50×10^{-9}	Section 3.6.2 (b)
IN17	$\text{H}_3\text{O}^+ + \text{H}_2\text{O} + \text{M}$	$\text{M}^+_{\text{CLUS}} + \text{M}$	1.00×10^{-27}	Section 3.6.3 (c)
IN18	$M_{\text{HPA}}\text{H}^+ + \text{H}_2\text{O} + \text{M}$	$\text{M}^+_{\text{CLUS}} + \text{M}$	1.00×10^{-27}	Section 3.6.3

Notes. The listed rate coefficients are the values at 300 K. For binary reactions the unit of the rate coefficient is $\text{cm}^3 \text{s}^{-1}$, whereas for the three-body reactions IN17 and IN18, the unit is $\text{cm}^6 \text{s}^{-1}$. Temperature dependencies of $(T/300)^{-0.5}$ are applied to all binary reactions with H_2O or M_{HPA} as the neutral reactant. For IN17 and IN18 we employ temperature dependencies of $(T/300)^{-4.0}$.

^a The products of the reaction were reported as HOC^+ (2/3) and HCO^+ (1/3), but here we assume that HOC^+ and HCO^+ have similar chemistry.

^b M_{HPA} denote molecules with higher proton affinity than H_2O (e.g., NH_3 and CH_3OH), and $M_{\text{HPA}}\text{H}^+$ are their protonated versions.

^c M is H_2O , CO , or M_{HPA} , and M^+_{CLUS} denote cluster ions such as $(\text{H}_2\text{O})_2\text{H}^+$ or $M_{\text{HPA}}\text{H}^+(\text{H}_2\text{O})$.

Table 2
Ion–Neutral Reactions between H_3O^+ and Selected Molecules Observed in Cometary Comae

Reactants	PA of Neutral (eV)	Dipole Moment of Neutral (D)	Products	300 K Rate Coefficient ($\text{cm}^3 \text{s}^{-1}$)
$\text{H}_3\text{O}^+ + \text{CH}_3\text{OH}$	7.82	1.69	$\text{CH}_3\text{OH}_2^+ + \text{H}_2\text{O}$	2.80×10^{-9}
$\text{H}_3\text{O}^+ + \text{NH}_3$	8.84	1.42	$\text{NH}_4^+ + \text{H}_2\text{O}$	2.40×10^{-9}
$\text{H}_3\text{O}^+ + \text{HCN}$	7.39	2.98	$\text{HCNH}^+ + \text{H}_2\text{O}$	3.50×10^{-9}
$\text{H}_3\text{O}^+ + \text{H}_2\text{S}$	7.38	0.97	$\text{H}_3\text{S}^+ + \text{H}_2\text{O}$	1.90×10^{-9}
$\text{H}_3\text{O}^+ + \text{CH}_3\text{CN}$	8.08	3.92	$\text{CH}_3\text{CNH}^+ + \text{H}_2\text{O}$	4.70×10^{-9}
$\text{H}_3\text{O}^+ + \text{HCOOH}$	7.69	1.41	$\text{HC}(\text{OH})_2^+ + \text{H}_2\text{O}$	2.70×10^{-9}
$\text{H}_3\text{O}^+ + \text{CH}_3\text{CHO}$	7.96	2.70	$\text{CH}_3\text{CHOH}^+ + \text{H}_2\text{O}$	3.60×10^{-9}

Notes. The reactions rates are from Mackay et al. (1979). Shown are also proton affinities (PA) and the permanent electric dipole moments of the neutrals as retrieved from the literature ($\text{PA}(\text{H}_2\text{O}) = 7.16 \text{ eV}$).

of the H_2O outgassing rate (e.g., Bockelée-Morvan et al. 2000; Ehrenfreund & Charnley 2000, and references therein; Crovisier et al. 2009; Biver et al. 2012). All of these molecules have higher proton affinities than H_2O and offer a loss mechanism for H_3O^+ . We list in Table 2 the 300 K rate coefficients determined experimentally for the proton transfer from H_3O^+ to a selection of neutral molecules that have been observed previously in cometary comae.

We consider at present only a single type of high proton affinity molecule, M_{HPA} , which we assume to be reactive with H_3O^+ to produce $M_{\text{HPA}}\text{H}^+ + \text{H}_2\text{O}$ with a 300 K rate coefficient of $2.50 \times 10^{-9} \text{ cm}^3 \text{ s}^{-1}$ as justified from the values in Table 2 (in particular from the values reported for the proton transfer reactions to NH_3 and CH_3OH). We assume a temperature dependence of $(T/300)^{-0.5}$ for these reactions as the listed neutral species all have fairly high permanent dipole moments (see Table 2 and Woodall et al. 2007). If the number density of M_{HPA} is at the level of few percent, or less, of the H_2O number density throughout the diamagnetic cavity, it is not needed to consider reactions of primary ions with M_{HPA} in the model as

these would still react primarily with the abundant H_2O . In addition, while the inclusion of M_{HPA} affects the ion chemistry and therefore the ion composition, it has a negligible effect on the electron production rates and only a small effect on the electron-loss rates (see Sections 3.7 and 5.7).

3.6.3. Loss of Abundant Ions through Cluster Ion Formation

Near the cometary surface the number density of neutral molecules may be sufficient for three-body cluster ion formation to be non-negligible. We assume that cluster ions, M^+_{CLUS} , are formed via the three-body reactions $\text{H}_3\text{O}^+ + \text{H}_2\text{O} + \text{M}$ (IN17 in Table 1) and $M_{\text{HPA}}\text{H}^+ + \text{H}_2\text{O} + \text{M}$ (IN18 in Table 1) with a three-body rate coefficient of $1.00 \times 10^{-27} \times (T/300)^{-4.0} \text{ cm}^6 \text{ s}^{-1}$, where M is a neutral molecule (H_2O , CO , or M_{HPA}). The selected rate coefficient is based on experimental investigations into three-body reactions by, e.g., Chatterjee & Johnsen (1987), Smith & Spanel (2001), and Hamon et al. (2005). At a later stage, the code may be updated to take into account formation of specified cluster ions and to take into account the M -dependence

Table 3
Dissociative Recombination (DR) Reactions Considered in the Model

Reaction	Reactants	Rate Coefficient ($\text{cm}^3 \text{s}^{-1}$)	Reference
DR1	$\text{H}_3\text{O}^+ + e^-$	$7.60 \times 10^{-7} \times (T_e/300)^{-0.83}$	Neau et al. (2000)
DR2	$\text{H}_2\text{O}^+ + e^-$	$4.30 \times 10^{-7} \times (T_e/300)^{-0.5}$	Rosén et al. (2000)
DR3	$\text{OH}^+ + e^-$	$3.75 \times 10^{-8} \times (T_e/300)^{-0.5}$	Mitchell (1990)
DR4	$\text{HCO}^+ + e^-$	$2.40 \times 10^{-7} \times (T_e/300)^{-0.69}$	Mitchell (1990)
DR5	$\text{CO}^+ + e^-$	$2.75 \times 10^{-7} \times (T_e/300)^{-0.55}$	Rosén et al. (1998)
DR6	$\text{H}_2^+ + e^-$	$1.60 \times 10^{-8} \times (T_e/300)^{-0.43}$	Mitchell (1990)
DR7	$M_{\text{HPA}}\text{H}^+ + e^-$	$9.00 \times 10^{-7} \times (T_e/300)^{-0.60}$	See Section 3.7
DR8	$M^+_{\text{CLUS}} + e^-$	$2.00 \times 10^{-6} \times (T_e/300)^{-0.50}$	See Section 3.7

Table 4
Description of Input Parameters of the Baseline Simulation at Perihelion (1.29 AU)

Parameter	Description
Cross sections for photo-processes	According to Section 3.3
Electron-impact cross sections	According to Section 3.4
Impinging solar EUV spectrum	See Figure 2(a)
Number densities of H_2O and CO	See Figure 1(a)
Mixing ratio of M_{HPA}	1%
Neutral temperature, T_n	See Figure 1(b) (temperature of H_2O)
Electron temperature, T_e	Same as T_n
Radial speed, u	See Figure 1(c) (radial speed of H_2O)
Rate coefficients for ion-neutral reactions	See Table 1 ^(a)
Rate coefficients for dissociative recombination reactions	See Table 3
Solar zenith angle	0°

Note. ^a Temperature dependencies are applied to the binary ion-neutral reactions involving H_2O (IN1, IN3–4, IN6–12, IN15) or M_{HPA} (IN16) as the neutral reactant and to the two considered three-body reactions (IN17–18), where the reactions are given in Table 1.

(see, e.g., Hamon et al. 2005) on the rate coefficient for cluster ion formation. As further chemical reactions of cluster ions with neutral reactants mainly lead to larger cluster ions, the M^+_{CLUS} ions are terminal species in our model that are only lost chemically by dissociative recombination with free thermal electrons.

3.7. Dissociative Recombination Reactions

Radiative recombination reactions of atomic ions (C^+ , H^+ , and O^+) with free thermal electrons have low rate coefficients (in the order of $\sim 10^{-12} \text{ cm}^3 \text{ s}^{-1}$) and are neglected. These atomic ions are rapidly lost through ion-neutral reactions (see Table 1). The dissociative recombination rate coefficients used for the various molecular ions included in our model are shown in Table 3. The selection of rate coefficient for the dissociative recombination of $M_{\text{HPA}}\text{H}^+$ (DR7 in Table 3) is based on the values reported for the dissociative recombination of CH_3OH_2^+ (Geppert et al. 2006) and NH_4^+ (Öjekull et al. 2004): $8.90 \times 10^{-7} \times (T_e/300)^{-0.59}$ and $9.43 \times 10^{-7} \times (T_e/300)^{-0.60} \text{ cm}^3 \text{ s}^{-1}$, respectively. The reasons to base the value on these two ions are (1) that CH_3OH has been observed in higher abundances than other candidate M_{HPA} molecules in the comae of other comets (see, e.g., Table 2 of Ehrenfreund & Charnley 2000) and (2) that NH_3 has the highest proton affinity among the molecules listed in Table 2 of this work, implying that proton transfer reactions effectively can increase the abundance of NH_4^+ at the expense of other $M_{\text{HPA}}\text{H}^+$ ions. The selection of rate coefficient for the dissociative recombination of M^+_{CLUS} is based on the values measured for a series of proton-bound dimer ions by McLain & Adams (2009).

4. RESULTS FROM THE BASELINE SIMULATION AND COMPARISONS WITH OTHER STUDIES

The baseline simulation is associated with conditions given in Table 4.

4.1. Electron and Primary Ion Production Rates

4.1.1. Electron and Primary Ion Production Rates from the Baseline Simulation

The relative yields of the ions H_2O^+ , OH^+ , O^+ , H^+ , H_2^+ , CO^+ , and C^+ produced through photoionization and through electron-impact ionization are roughly constant with cometocentric distances (at least for $r > 5 \text{ km}$) with values of 100, 20–22, 1.5–2, 9–10, 0.001–0.004, 7–8, and 0.4–0.6, respectively (baseline simulation). It is noted that, e.g., OH^+ can be produced in cometary coma by the photoionization of OH (formed by the photodissociation of H_2O), but the focus here is mainly on major ions and electrons. The calculated electron production rates due to photoionization and electron-impact ionization are shown versus cometocentric distance in Figure 5(a), while the primary efficiency, defined as the ratio of the electron-impact ionization rate to the photoionization rate, is displayed in Figure 5(b). The results from the baseline simulation are shown with solid lines, along with the electron production rate due to electron impact ionization derived with the electron-impact electronic excitation cross sections of H_2O divided by a factor of 10 (dashed lines). In Section 3.4.2, we highlighted that these cross sections are somewhat uncertain judging from the spread in experimental and theoretical determinations, and that the cross section used in the baseline simulation is significantly higher than the sum of the cross sections for excitations into individual

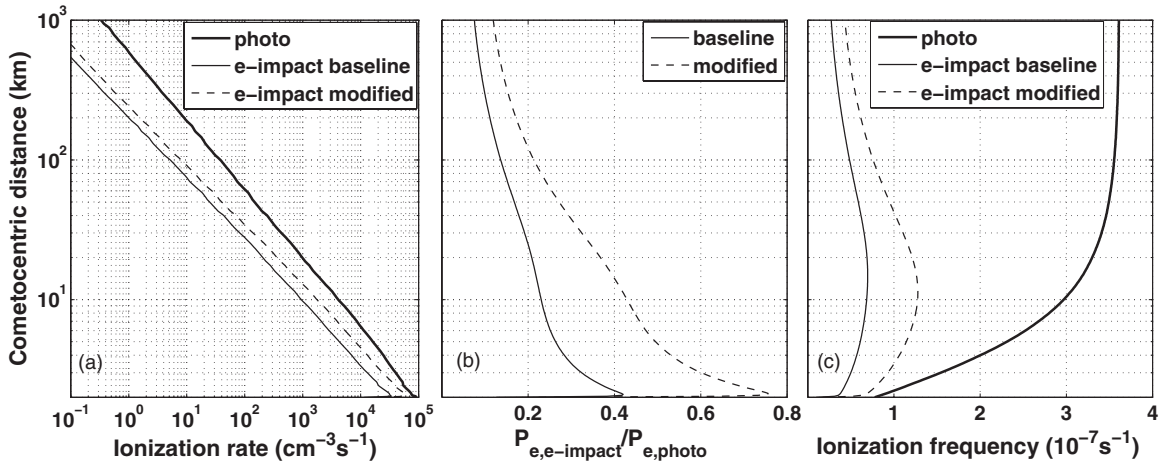


Figure 5. (a) Calculated electron-impact rates and photoionization rates, (b) primary efficiency, and (c) photoionization and electron-impact ionization frequencies vs. cometocentric distance. Shown by solid lines are results from the baseline simulation, while dashed lines show results from a modified simulation in which the cross section for the electronic excitation of H_2O was divided by 10.

states presented in Thorn (2008). The effect on the total electron production rate is rather small; at $r = 100$ km P_e is increased by $\sim 7\%$ and closer to the surface the increase amounts to $\sim 16\%$ following the modification of the cross section for the electron impact electronic excitation of H_2O . The enhanced effect toward lower cometocentric distances can be explained by the fact that the relative importance of electron-impact ionization to the total electron production rate increases with decreasing cometocentric distance (as seen in Figure 5(b)). This is in turn because the photo-absorption cross sections for H_2O and CO decrease with decreased wavelength (see Figure 3), such that following the attenuation of the solar irradiation toward lower cometocentric distances the released photoelectrons have higher kinetic energies on average.

The photoionization rate, or the photoelectron production rate, $P_{e,\text{photo}}(r)$ can be reasonably (within 10%) fitted by the following function for $r > 10$ km:

$$P_{e,\text{photo}}(r) = 3.8 \times 10^5 \times r^{-2}, \quad (9)$$

where $P_{e,\text{photo}}$ and r are in units of $\text{cm}^{-3} \text{s}^{-1}$ and km, respectively. The $1/r^2$ dependence reflects the optically thin medium properties (for $r > 10$ –20 km) and the $1/r^2$ dependence of the neutral number densities at $r > 10$ km (see Section 3.1). We have calculated the cometocentric distance $r_{\text{dep}}(\lambda)$ where the energy deposition rate of photons of wavelength λ is highest. The $r_{\text{dep}}(\lambda)$ values versus λ are shown in Figure 6 for three different simulations: the baseline simulation and simulations with two and four times enhanced neutral number densities. In the baseline simulations, the energy deposition rates of photons with $\lambda < 52$ nm do not peak above the surface, while the deposition rates for photons with $52 \text{ nm} < \lambda < 75$ nm and $83 \text{ nm} < \lambda < 93$ nm peak just above the surface due to the higher photoabsorption cross sections in these wavelength regimes (see Figure 3). For the simulations with two and four times enhanced neutral number densities the energy deposition rates peak above the surface for photons with $\lambda > 30$ nm and $\lambda > 20$ nm, respectively.

The photoionization and electron-impact ionization frequencies for neutral molecules (calculated as the ionization rates divided by the total neutral number density) are shown in Figure 5(c). These ionization frequencies are similar (to within a few percent) to those for H_2O alone. The assumption of a constant ionization frequency throughout the cometary coma

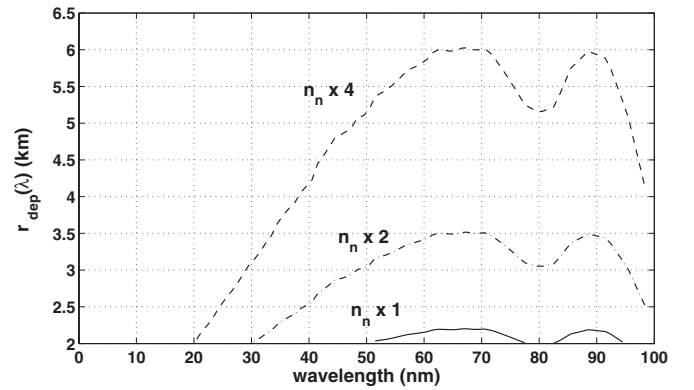


Figure 6. Cometocentric distance, $r_{\text{dep}}(\lambda)$, where the energy deposition rate of photons of wavelength λ is maximal. The solid line shows results from the baseline simulation, while the dash-dotted and dashed lines show results from simulations with two and four times enhanced neutral number densities, respectively.

is not appropriate, at least not for cometocentric distances below 10–20 km, where the atmosphere starts to become optically thick to solar EUV radiation. The photoionization frequency for $r > 10$ km ranges from ~ 3.0 to $3.6 \times 10^{-7} \text{ s}^{-1}$ (non-attenuated value), while for lower r the values decrease rapidly.

4.1.2. Comparison with Ionization Rates from Other Studies

Ionization rates depend strongly on the neutral number densities and the impinging solar EUV spectrum and have, to the best of our knowledge, not been reported previously for 67P/CG at perihelion. For a comparison with the literature it is therefore suitable to use input parameters similar to published studies in terms of neutral number densities and impinging solar EUV spectrum.

First of all, we have run our model assuming similar circumstances as Bhardwaj (2003): solar minimum conditions, heliocentric distance of the comet of 1 AU with an H_2O outgassing rate of 1×10^{28} molecules s^{-1} , and with H_2O densities calculated according to Bhardwaj et al. (1990). For solar minimum conditions we used the TIMED/SEE spectrum from 2008 January 20. On the one hand, our derived photoelectron production rates were found to be in good agreement with the ones

Table 5
Photoionization Frequencies of H₂O Derived through Different Studies for a Heliocentric Distance of 1 AU under Solar Minimum and Maximum Conditions

Reference	Photoionization Frequency (10^{-7} s^{-1})	
	Solar Minimum	Solar Maximum
Present study (at 600 km)	4.2	9.2 ^a
Körözmezey et al. (1987)	3.8	10.5
Crovisier (1989)	4.0	8.7
Huebner et al. (1992)	4.1	10.4
Budzien et al. (1994)	5.2 ± 2	11.6 ± 2

Notes. (a) We have tested a few different spectra corresponding to solar maximum conditions and obtained H₂O photoionization frequencies ranging from 9.0 to $10.2 \times 10^{-7} \text{ s}^{-1}$ at $r = 600 \text{ km}$.

calculated by Bhardwaj (2003), typically only 10%–15% higher. On the other hand, Bhardwaj (2003) predicted primary efficiencies of about 0.6–0.7 even at large cometocentric distances, significantly higher than suggested from our model calculations. In our simulation, $P_{e,e\text{-impact}}/P_{e,\text{photo}}$ have values ranging from about 0.08 to 0.15 for $r > 100 \text{ km}$. If we divide the cross section for electronic excitation of H₂O by 10, the primary efficiency increases, but by less than a factor of two (the reason for the increase being the increased probability for a suprathermal electron to degrade in kinetic energy by causing ionization). It is not clear for us what causes the very high primary efficiencies derived by Bhardwaj (2003). During solar minimum conditions Körözmezey et al. (1987) derived for a Halley-type comet at 1 AU (cometocentric distance of 4650 km where the H₂O number density was about $3 \times 10^6 \text{ cm}^{-3}$) a primary efficiency of ~ 0.08 (~ 0.18) for a simulation including (excluding) photoelectron transport. When running our model for a Halley-type comet under solar minimum conditions at 1 AU and with a similar H₂O number density profile as used by Körözmezey et al. (1987) we find primary efficiencies of ~ 0.13 (photoelectron transport included) and ~ 0.21 (photoelectron transport excluded) at 4650 km.

When applying solar minimum and solar maximum conditions to our baseline simulation of 67P/CG, we find H₂O photoionization frequencies of $\sim 2.6 \times 10^{-7} \text{ s}^{-1}$ and $5.5 \times 10^{-7} \text{ s}^{-1}$, respectively, at a cometocentric distance of 600 km. The corresponding values for a heliocentric distance of 1 AU, as obtained by scaling with an $1/R^2$ dependence (R being the heliocentric distance), are $4.2 \times 10^{-7} \text{ s}^{-1}$ and $9.2 \times 10^{-7} \text{ s}^{-1}$, respectively. These values can be compared with a number of previous results as shown in Table 5. Our results are in good agreement with the earlier studies. The small differences found may be explained by small dissimilarities in the utilized solar EUV spectra and/or photo cross-section sets. We have tested a few different EUV spectra corresponding to solar maximum conditions and obtain values for the unattenuated photoionization frequency of H₂O ranging from 9.0 to $10.2 \times 10^{-7} \text{ s}^{-1}$.

4.2. Timescales for Transport and Chemical Processes

Figure 7 shows (based on results from our baseline simulation) the chemical timescales of thermal electrons H₂O⁺, H₃O⁺, and $M_{\text{HPA}}\text{H}^+$ given by $t_{\text{chem},j}(r) = 1/L_j(r)$ versus cometocentric distance as well as the transport (advection) timescale for the species given by $t_{\text{adv}}(r) \sim r \times [2u(r)]^{-1}$ where u is the bulk radial speed of the dominant water molecules.

The chemical timescales for H₂O⁺ and $M_{\text{HPA}}\text{H}^+$ can be very well approximated by the timescales for the proton transfer reaction from H₂O⁺ to H₂O (IN1) and the dissociative recom-

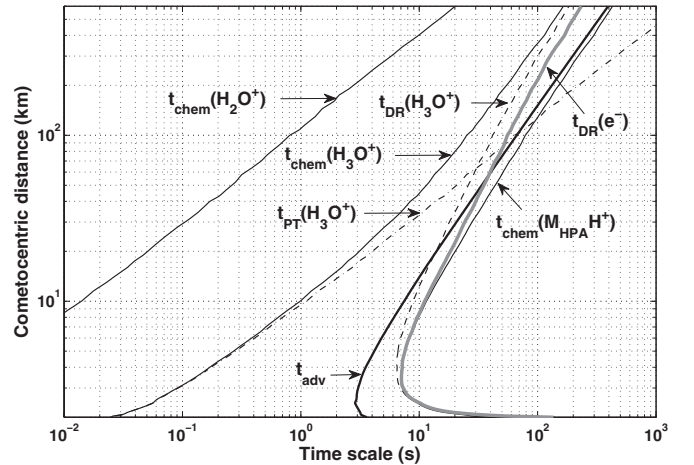


Figure 7. Timescales for advection, t_{adv} , the dissociative recombination of electrons, $t_{\text{DR}}(e^-)$, and the chemical losses, t_{chem} , of H₂O⁺, H₃O⁺, and $M_{\text{HPA}}\text{H}^+$ based on the results from the baseline simulation. For H₃O⁺ the timescales for dissociative recombination (DR) and proton transfer (PT) to M_{HPA} are also shown.

bination of $M_{\text{HPA}}\text{H}^+$ (DR7), respectively. Photochemical equilibrium holds for H₂O⁺ over the whole region considered (as $t_{\text{chem}}(\text{H}_2\text{O}^+) \ll t_{\text{adv}}$) and is also a good approximation for H₃O⁺ in the presence of M_{HPA} , at least below 30 km. For H₃O⁺, we show in Figure 7 the specific timescales for dissociative recombination and proton transfer to M_{HPA} . Roundabout 70 km these timescales are similar, whereas below (above) 70 km the timescale for dissociative recombination is longer (shorter) than for the proton transfer to M_{HPA} . Photochemical equilibrium is not a very good approximation for $M_{\text{HPA}}\text{H}^+$, the chemical timescale of which is longer than the advection timescale.

The advection timescale is of the same order as the chemical timescale for the loss of thermal electrons due to dissociative recombination, $t_{\text{DR}}(e^-)$, over the whole region studied, implying that photochemical equilibrium does not hold for the electrons. In addition, advection becomes the dominant process for cometocentric distances below $\sim 50 \text{ km}$, with the relative difference between t_{adv} and $t_{\text{DR}}(e^-)$ increasing toward the surface. This is largely due to the thermal electron temperature profile, with lower temperatures toward higher cometocentric distances, which significantly affects the loss rate for dissociative recombination. We have run a simulation with a constant electron temperature of 15 K. The resulting recombination timescales were for $3 \text{ km} < r < 300 \text{ km}$ always within 10% of the advection timescales (and the peak electron number density was decreased by 25% compared with the baseline simulation).

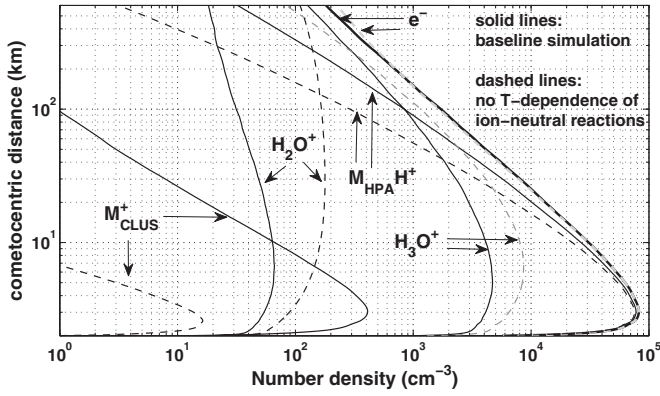


Figure 8. Solid lines: number densities of electrons H_2O^+ , H_3O^+ , $M_{\text{HPA}}\text{H}^+$, M^+_{CLUS} vs. cometocentric distance as calculated through the baseline simulation (negative temperature dependencies of ion–neutral reactions that involve H_2O or M_{HPA} as neutral reactant). Dashed lines: the same but from a simulation in which the temperature dependencies were disregarded for all ion–neutral reactions.

4.3. Number Densities of Thermal Electrons and Selected Ions and Comparison with Other Studies

The calculated number densities, using the baseline simulation, of thermal electrons H_2O^+ , H_3O^+ , M^+_{CLUS} (see Section 3.6.3), and $M_{\text{HPA}}\text{H}^+$ (see Section 3.6.2) are shown versus cometocentric distance in Figure 8 by solid lines. The maximum abundances of the minor ion species OH^+ , CO^+ , HCO^+ , H^+ , O^+ , C^+ , and H_2^+ (not shown in the figure) are ~ 7.8 , 3.2 , 1.7 , 1.6 , 0.6 , 0.2 , and 0.001 cm^{-3} , respectively. Shown in Figure 8 by dashed lines are also the results from a simulation run in which the temperature dependencies of all ion–neutral reactions were disregarded. This action does not have a prominent influence on the derived thermal electron number density but affects the calculated number densities of the various ions. We return to these effects shortly but discuss first the results for the baseline simulation.

The thermal electron number density peaks at a value of $\sim 8 \times 10^4 \text{ cm}^{-3}$ at $\sim 1 \text{ km}$ above the surface (see Figure 8), despite that P_e is highest in the very vicinity of the surface (see Figure 5(a)). This is related to the more pronounced negative values of the flux divergence term at low distances from the surface (in the very vicinity of the surface there is no ion inflow from below). This finding comes as no surprise. Mendis et al. (1981) appointed that the electron number density, in a spherical symmetric inner ionosphere of a comet, is expected to peak roundabout a cometary radius above the surface.

In an atmosphere where photochemical equilibrium prevails and where the effective recombination coefficient is constant with altitude, n_e is proportional to the square root of P_e . With a $1/r^2$ dependence of P_e (as in Equation (9)) this yields a $1/r$ dependence of n_e . These characteristics are, however, not applicable for our model of 67P/CG, as advection plays a critical role in the continuity equations for the ions and as the effective recombination coefficient changes drastically with cometocentric distance following primarily the changes in the electron temperature (see Figure 1(b)). We find that the thermal electron number density for $r > 10 \text{ km}$ instead roughly (within 10%) follows the relation

$$n_e = 5.1 \times 10^5 \times r^{-1.23}, \quad (10)$$

where n_e and r are in units of cm^{-3} and km , respectively.

The peak electron number density matches at least within 20% the calculations for 67P/CG at perihelion by Benna & Mahaffy (2006, see their Figure 4), though we are not certain regarding exactly what input parameters (e.g., the neutral number density profile and solar flux) were used in their multi-fluid MHD model. Our predicted maximum electron number density is about a factor of seven higher compared with the peak value shown in Figure 6.13 of von Oertzen (2003). The pronounced difference is mainly explained by the fact that von Oertzen applied a constant radial speed of 1 km s^{-1} (higher value compared with present study, see Figure 2(c)), which (1) reduces the neutral number densities (inversely proportional to u) and (2) increases the importance of advection compared with our model. We have tested the approach by von Oertzen (2003) applying the same neutral number densities and (constant) ionization frequency and successfully reproduced his results. The radial speed u needs to be decreased from a value of 1 km s^{-1} to approximately 0.35 km s^{-1} (which in that model increases the neutral densities and reduces the advection timescale) in order to retrieve a maximal n_e value equal to that given by our baseline simulation shown in Figure 8 ($\sim 8 \times 10^4 \text{ cm}^{-3}$).

As shown in Figure 8, $M_{\text{HPA}}\text{H}^+$ (ions such as CH_3OH_2^+ , NH_4^+ , etc.) becomes dominant at cometocentric distances below $\sim 90 \text{ km}$ in the baseline simulation. Many previous ionospheric models of comets (e.g., von Oertzen 2003; Benna & Mahaffy 2006) exclude other ions than H_3O^+ and H_2O^+ . Other models, aimed in particular at reproducing ion densities observed in the coma of comet 1P/Halley during the *Giotto* mission, have focused on large cometocentric distances, where water group ions still are dominant (e.g., Rubin et al. 2009). Several authors (e.g., Marconi & Mendis 1988; Ip 1989; Haider & Bhardwaj 2005) have found that NH_4^+ should be the dominant ion within a few 100 km from the nucleus of 1P/Halley (heliocentric distances of 0.9–1.0 AU), given only a low mixing ratio of NH_3 (between 0.3% and 1.5%). It seems, however, as if these authors, at least Marconi & Mendis (1988) and Haider & Bhardwaj (2005), did not consider a negative temperature dependence of the proton transfer reaction from H_3O^+ to NH_3 , which would have shifted the cometocentric distance, below which NH_4^+ becomes dominant, upward (see dashed lines and solid lines in Figure 8 and Section 5.7).

The cluster ions in our baseline simulation reach only a maximum number density of $\sim 4 \times 10^2 \text{ cm}^{-3}$, a few kilometers above the cometary surface. Increasing (decreasing) the rate coefficients of IN17 and IN18 by an order of magnitude increases (decreases) the maximum number density by a factor close to 10. The associated decrease (increase) of the number densities of H_3O^+ and $M_{\text{HPA}}\text{H}^+$ is negligible in a relative sense, the maximum changes being within 0.5%. The nearly linear relation between the peak abundance of M^+_{CLUS} and the rate coefficients used for IN17 and IN18 follows from the facts that (1) IN17 and IN18 are the only production sources for M^+_{CLUS} and (2) in the region close to the surface the removal of ions is largely controlled by advection (see the timescales for electron recombination and advection in Figure 7).

We shall now briefly discuss the differences between the results from the baseline simulation and the results from the simulation in which the temperature dependencies of all ion–neutral reactions were neglected (see Figure 8). The differences for H_2O^+ and $M_{\text{HPA}}\text{H}^+$ become more and more pronounced with increased cometocentric distance, which is due to the neutral temperature profile (Figure 1(b)), with reduced temperatures toward higher r . Following the removal of the T -dependencies the

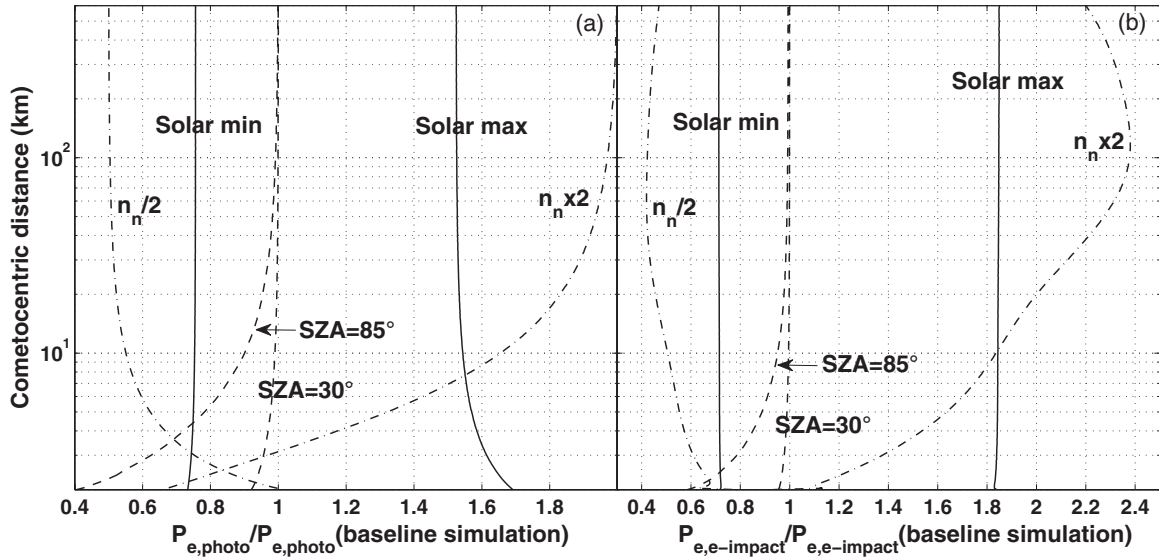


Figure 9. Effect on (a) $P_{e,photo}$ and (b) $P_{e,e-impact}$ following changes in input parameters of the baseline simulation: impinging solar EUV spectrum (solid lines), neutral number densities (dash-dotted lines), and solar zenith angle (dashed lines).

H_2O^+ density increases as it becomes longer lived against being lost through the reaction IN1: $H_2O^+ + H_2O \rightarrow H_3O^+ + OH$. At the same time, the number density of $M_{HPA}H^+$ is reduced as the rate coefficient for IN16: $H_3O^+ + M_{HPA} \rightarrow M_{HPA}H^+ + H_2O$ decreases. For H_3O^+ the decreased production due to IN1 is counterbalanced by the decreased loss due to IN16, and it is seen that at $r \sim 200$ km the H_3O^+ number densities calculated from the two simulations match each other. The fact that M^+_{CLUS} is so heavily depleted already at low cometocentric distances is related to the strong negative temperature dependence of $(T/300)^{-4.0}$ for IN17 and IN18 used in the baseline simulation.

5. SENSITIVITY TESTS

In Section 5, we test how the predicted photoelectron production rates and number densities of thermal electrons and major ions change following changes to different input parameters of the model. Comparisons are made to the results from the baseline simulation, and in each sensitivity test (if not otherwise stated) only a single parameter is altered. Effects on the electron production rates are shown in Figures 9(a) (photoionization) and (b) (electron-impact ionization) and on the thermal electron number densities in Figure 10 as well as in Table 6 for a few selected cometocentric distances. Figure 11 illustrates how the ratio, between the number densities of $M_{HPA}H^+$ and electrons, changes with the mixing ratio of M_{HPA} and the temperature dependence of the ion-neutral reaction $H_3O^+ + M_{HPA} \rightarrow M_{HPA}H^+ + H_2O$ (IN1).

5.1. Change of the Impinging Solar EUV Spectrum

We have tested two extreme scenarios for the impinging solar EUV spectra. They correspond to solar maximum and solar minimum conditions, with $F_{10.7}$ values of 174 and $70 \times 10^{22} \text{ Wm}^{-2} \text{ Hz}^{-1}$, respectively (see Figure 2). The effects of using these spectra on the predicted photoelectron production rates and the n_e values are shown in Figure 9(a) (solid lines) and Figure 10(a), respectively. As expected, the ionization rates increase with increasing solar activity. Below we discuss only the effects of using the solar maximum spectrum, as the effects seen for the solar minimum simulation can be explained

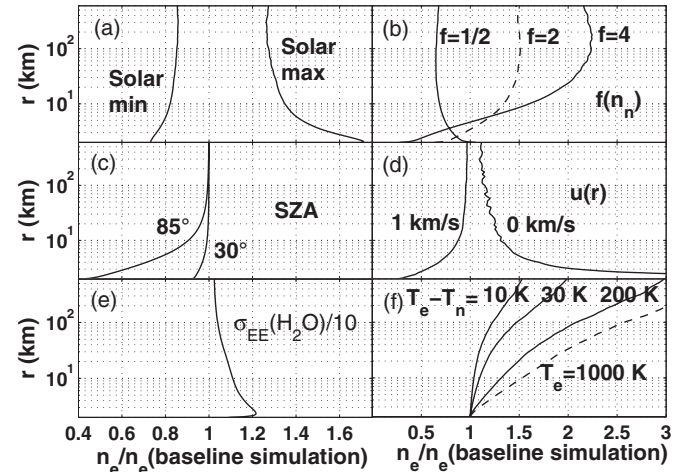


Figure 10. Effect on n_e following changes of input parameters of the baseline simulation. The different panels show the effects of changing (a) the impinging solar EUV spectrum, (b) the neutral number densities by a factor of $f(n_n)$, (c) the solar zenith angle, (d) the radial speed of the species, (e) the electron-impact electronic excitation cross section of H_2O , and (f) the electron temperature profile.

analogously, though these effects are more modest, following a more modest difference in solar flux (see Figure 2(b)).

Noteworthy there is an enhanced effect on $P_{e,photo}$ at low cometocentric distances ($r < 7$ km), for the solar maximum case. This is due to two combined effects: (1) the structure of the photoabsorption cross sections of H_2O and CO (see Figure 3) causes a non-negligible fraction of the photons with wavelengths longer than 50 nm to start to be absorbed above $r \sim 7$ km (therefore, the relative abundance of photons with wavelengths below 50 nm increases with decreasing r), and (2) the EUV spectrum for the solar maximum case is particularly enhanced below 50 nm (see Figure 2(b)). The rather prominent increase of the ratio n_e/n_e (baseline simulation) toward low cometocentric distances follows from the behavior of $P_{e,photo}$ and the fact that in this transport-dominated region (see the timescales in Figure 7) n_e scales more linearly to P_e .

Table 6

Effect on n_e Following Changes of Input Parameters of the Baseline Simulation at Cometocentric Distances of 5, 10, 30, and 70 km, where the n_e Values Given by the Baseline Simulation are 6.29×10^4 , 3.08×10^4 , 8.07×10^3 , and $2.68 \times 10^3 \text{ cm}^{-3}$, Respectively

Change	Figure	$n_e/n_e(\text{Baseline Simulation})$			
		5 km	10 km	30 km	70 km
Solar minimum	10(a)	0.79	0.82	0.84	0.85
Solar maximum	10(a)	1.43	1.35	1.30	1.28
$n_n \times 1/2$	10(b)	0.74	0.69	0.65	0.65
$n_n \times 2$	10(b)	1.15	1.34	1.47	1.50
$n_n \times 4$	10(b)	1.06	1.60	2.06	2.20
SZA = 30°	10(c)	0.98	0.99	1.00	1.00
SZA = 85°	10(c)	0.77	0.90	0.98	0.99
$u = 0 \text{ km s}^{-1}$	10(d)	1.52	1.31	1.20	1.15
$u = 1 \text{ km s}^{-1}$	10(d)	0.75	0.88	0.94	0.95
$\sigma_{EE}(\text{H}_2\text{O})/10$	10(e)	1.14	1.11	1.07	1.05
$\sigma_{\text{abs}} \times 1.2^a$...	1.00	1.07	1.10	1.10
$\sigma_{\text{abs}} \times 0.8^a$...	0.92	0.90	0.89	0.89
$T_e = T_n + 10 \text{ K}^b$	10(f)	1.02	1.04	1.09	1.18
$T_e = T_n + 30 \text{ K}^b$	10(f)	1.05	1.10	1.22	1.39
$T_e = T_n + 200 \text{ K}^b$	10(f)	1.16	1.32	1.60	1.93
$T_e = 1000 \text{ K}$	10(f)	1.27	1.53	1.95	2.38
$M_{\text{HPA}} 0.3\%^c$...	1.00	0.99	0.96	0.94
$M_{\text{HPA}} 5\%^c$...	1.00	1.01	1.03	1.07

Notes.

^a For these simulations the photoabsorption and all photoionization cross sections of H₂O and CO were changed by the given factor.

^b T_n is the kinetic temperature of H₂O seen in Figure 1(b).

^c For these simulations the mixing ratio of M_{HPA} was set to 0.3% and 5%, while in the baseline simulation it is set to 1%.

Following the use of solar maximum conditions the relative increase of the electron-impact ionization rates is somewhat higher than that of the photoelectron production rates. This is because the solar spectrum is especially enhanced toward lower wavelengths, with the photoionization events leading to higher photoelectron energies on average. The ejected photoelectrons at 100 km have an average energy of roughly 15 eV for the baseline simulation and 17 eV for the solar maximum simulation. At about 3 km the corresponding values are ~ 20 eV (baseline simulation) and 22 eV (solar maximum simulation). Comparing the solar maximum case with the baseline simulation, the relative difference between the average energy of the ejected photoelectrons decreases slowly with decreasing cometocentric distance, which results in the decreasing trend of $P_{e,e\text{-impact}}/P_{e,e\text{-impact}}$ (baseline simulation) for the solar maximum simulation (visible toward low cometocentric distances in Figure 9(b)).

5.2. Change of Neutral Number Densities

In Figures 9(a) and (b) (by dash-dotted lines), we show the effect on $P_{e,\text{photo}}$ and $P_{e,e\text{-impact}}$ of multiplying by 2, or dividing by 2, the number densities of H₂O and CO. M_{HPA} has its volume mixing ratio held constant at 1%. At high cometocentric distances, the photoelectron production rates are seen to scale with the neutral densities (optically thin atmospheres), but toward distances closer to the surface the effects of photoabsorption become apparent, yielding a larger and larger increase (decrease) of $P_{e,\text{photo}}$ with decreasing r , as the neutral densities are decreased (increased) with respect to the baseline simulation. When the neutral number density is increased, the photons are absorbed at higher cometocentric distances as illustrated in Figure 6. In that case, the effect on

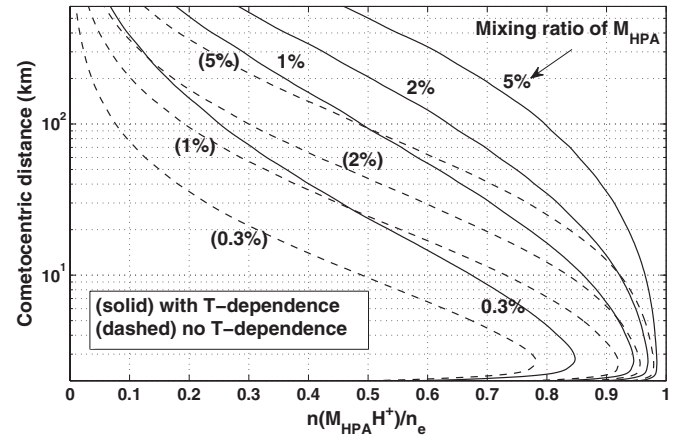


Figure 11. Predicted relative abundance of $M_{\text{HPA}}\text{H}^+$ with respect to electrons vs. cometocentric distance for different values of the mixing ratio of M_{HPA} . The solid (dashed) lines are for model runs where a negative temperature dependence of the ion–neutral reaction $\text{H}_3\text{O}^+ + M_{\text{HPA}} \rightarrow M_{\text{HPA}}\text{H}^+ + \text{H}_2\text{O}$ have been included (excluded).

photoionization rates becomes apparent at higher r compared with the baseline case.

The increased neutral number densities affect $P_{e,e\text{-impact}}$ even more than they affect $P_{e,\text{photo}}$ (Figures 9(a) and (b)). In the vicinity of the surface the primary efficiency is increased by about 40%–60% compared with the baseline simulation following an increase of the neutral densities by a factor of two. This follows mainly from the structure of the photoabsorption cross sections of H₂O and CO (see Figure 3), which decreases with decreased wavelength in particular for wavelengths below 30 nm. With increased neutral number densities the photoelectrons produced at a given r are, due to the attenuation effect in the column above r , more energetic on average. The increase of the primary efficiency is also in part due to the more local deposition of the associated photoelectrons in the more dense atmospheres.

The effect on the n_e prediction of changing the neutral number densities is shown in Table 6 and in Figure 10(b), where we also have included the case with four times enhanced number densities. A similar behavior as seen for the photoelectron production rate is observed.

5.3. Change of Solar Zenith Angle

We have made simulations with the SZA set to 30° and 85°. For simplicity all other parameters of the baseline simulation remained unchanged, including the background neutral densities. In Figures 9(a) and (b) (dashed lines) we show the effect on $P_{e,\text{photo}}$ and $P_{e,e\text{-impact}}$, and in Figure 10(c) we show the influence on the predicted thermal electron number densities. The consequence of increased SZA becomes apparent only at sufficiently low cometocentric distances. For SZA = 30° and 85° the effects are seen for $r < 10$ km and $r < 100$ km, respectively. The effect on $P_{e,\text{photo}}$ at $r = 10$ km of using SZA = 85° only yields a decrease by about 10% (see Table 6). This is in line with the studies by Bhardwaj (2003), who showed that the photoionization rates in low outgassing comets are not significantly influenced by increased SZA (at least not for SZA up to 120°). Increasing the SZA means that for a given r the atmospheric column is increased. As a result, the solar flux at r is only significantly reduced in the optically thick region close to the surface. The increased column densities have, however, a smaller effect on the penetration of photons with wavelengths

shortward of 30 nm, as the H₂O and CO photoabsorption cross sections are lower in that region of the spectrum (see Figures 3 and 6). As these photons produce more energetic photoelectrons, this leads to higher primary efficiencies toward the surface of the comet in comparison to the baseline simulation.

5.4. Change of Radial Speed of Ions

The electron production rates are independent of the radial speed. The electron density depends on it (Figure 10(d)) through the flux divergence term present in the continuity equation (Equation (5)). At the low extreme we have used $u(r) = 0 \text{ km s}^{-1}$, such that ion and electron number densities are given from photochemical equilibrium. We have also increased $u(r)$ to a constant value of 1 km s^{-1} as often assumed in model calculations of comets (e.g., Bhardwaj et al. 1990; von Oertzen 2003). The predicted thermal electron number densities decrease with increased $u(r)$. The effect is most apparent near the surface, where the timescale for advection becomes lower for the “ $u(r) = 1 \text{ km s}^{-1}$ model” compared with the baseline simulation (see Figure 7) and infinitely long for the photochemical equilibrium model.

5.5. Change of Photo- and Electron-impact Cross Sections

The ionization of the neutral constituents is dominated by photoionization (see Figure 5). Changes within 30% of the cross sections for electron-impact processes accordingly do not have a significant influence on the predicted electron number densities. A particular uncertain process in the electron-impact cross section set is the electronic excitation of H₂O as mentioned in Section 3.2.2. Dividing the cross section for this process by 10 gives the effect on the electron-impact ionization rate, as shown in Figure 5(a). The effect on the total electron production rate is smaller, and the thermal electron number densities are only predicted to be about 3%, 5%–11%, and 11%–20% higher than in the baseline simulation above 100 km, between 10 and 100 km, and below 10 km, respectively (see Figures 10(e) and Table 6). The increased electron number densities are due to the increased relative importance of ionization processes in the energy degradation of the suprathermal photoelectrons and their associated secondary electrons.

The photoionization cross sections used in the model are expected to be accurate to within approximately 20%. Increasing (decreasing) all of the photoionization and photoabsorption cross sections by 20% leads to increased (decreased) n_e values of about 10% (11%) at 70 km, and the effect becomes smaller toward lower cometocentric distances (see Table 6). The increased (decreased) cross sections even lead to decreased (enhanced) predictions of n_e below cometocentric distances of $\sim 5 \text{ km}$ ($\sim 3 \text{ km}$). This follows from the fact that increasing (decreasing) the photoabsorption cross sections makes the atmosphere optically thicker (thinner).

5.6. Change of Electron Temperature Profile

The electron production rates are independent of the electron temperature in the model, while the thermal electron number density is dependent on it through the T_e dependencies of the dissociative recombination reactions (see Section 3.7). We show in Figure 10(f) and Table 6 how n_e is affected by using T_e values that are 10, 30, and 200 K higher than the ambient neutral temperature (the kinetic temperature of H₂O seen in Figure 1(b)). We also show (by a dashed line) the effect of using a T_e profile at a constant value of 1000 K. As the efficiency

for dissociative recombination decreases with increased T_e , the predicted electron number densities increase with increased T_e . The effect is quite pronounced, even for electron temperatures elevated by 10 K with respect to the neutral temperature. The fact that the effect is most pronounced at high cometocentric distances is mainly related to the neutral temperature profile (see Figure 1(b)). Temperatures are higher at lower cometocentric distances, which means that the relative impact of elevated electron temperatures becomes more and more pronounced with increased cometocentric distance. The very small effect on T_e in the vicinity of the surface is a result of the increasing dominance of advection compared with dissociative recombination for the removal of free thermal electrons (see Figure 7).

5.7. Changes of Parameters Mainly Affecting the Ion Chemistry

In Figure 11 (solid lines), we show the $M_{\text{HPA}}\text{H}^+$ /electron number density ratio versus cometocentric distance predicted for model runs with different M_{HPA} mixing ratios. The predicted electron number densities versus cometocentric distance (not shown) do not differ much between these model runs as H₃O⁺ and $M_{\text{HPA}}\text{H}^+$ (in the model) have fairly similar rate coefficients for dissociative recombination (see Section 3.7). Even when increasing the mixing ratio of M_{HPA} to 5% the calculated electron number densities are always within 12% (within 7% below 80 km) of the values calculated through the baseline simulation. Increasing the volume mixing ratio of M_{HPA} naturally leads to a higher fractional abundance of $M_{\text{HPA}}\text{H}^+$ at a given r , as the production rate of $M_{\text{HPA}}\text{H}^+$ through the proton transfer reaction (IN16) $\text{H}_3\text{O}^+ + M_{\text{HPA}} \rightarrow M_{\text{HPA}}\text{H}^+ + \text{H}_2\text{O}$ increases.

We show also in Figure 11 (dashed lines) how the predicted relative abundance of $M_{\text{HPA}}\text{H}^+$ changes by removing the temperature dependence in the proton transfer reaction (IN16) $\text{H}_3\text{O}^+ + M_{\text{HPA}} \rightarrow M_{\text{HPA}}\text{H}^+ + \text{H}_2\text{O}$. It is seen that the temperature dependence has a pronounced influence on the predicted density of $M_{\text{HPA}}\text{H}^+$, especially at high r where the neutral temperature is low. For example, near $r = 50 \text{ km}$, where the neutral temperature is around 20 K, the rate coefficient for a proton transfer reaction is enhanced by a factor of ~ 4 when a $(T/300)^{-0.5}$ dependence is applied. As an interesting example, the r values below which $M_{\text{HPA}}\text{H}^+$ is the dominant ion are similar ($\sim 90 \text{ km}$) for the simulation “ M_{HPA} mixing ratio of 5%, no T -dependence of IN16,” and the baseline simulation in which the M_{HPA} volume-mixing ratio is 1% and a negative T -dependence is applied to IN16.

While any future model of the ion chemistry of 67P/CG may have a well-constrained parameter space (following *Rosetta* in situ measurements of neutral number densities and temperatures), it is clear that a good knowledge of low-temperature reaction rates is of pivotal importance for a better understanding of the ion chemistry within the diamagnetic cavity. This is further highlighted by the notable effects on the ion chemistry of removing the temperature dependence of all ion–neutral reactions considered in the model (see Figure 8).

6. CONCLUSIONS

We have predicted the ionization rates and number densities of thermal electrons and selected ions versus cometocentric distance, r , under solar illumination for the diamagnetic cavity of comet 67P/Churyumov–Gerasimenko near perihelion at 1.29 AU. The parameters of the baseline simulation are given in Table 4, and negative temperature dependencies were applied to all ion–neutral reactions involving H₂O or M_{HPA} (molecules with higher proton affinity than H₂O) as the neutral reactant.

The main results from the baseline simulation are summarized as follows.

1. The electron production rate increases with decreased cometocentric distance. The dominant contribution to the total electron production rate is the photoelectron production rate, which for $r > 10$ km is well fitted by a $1/r^2$ dependence (see Equation (9)). The most important primary ions are H_2O^+ , OH^+ , H^+ , CO^+ , O^+ , and C^+ , which are formed at relative yields of 100, 20–22, 9–10, 7–8, 1.5–2, and 0.4–0.6, respectively. The primary efficiency, which is defined as the ratio $P_{e,e\text{-impact}}/P_{e,\text{photo}}$, ranges from about 0.1 to 0.4 (see Figure 5(b)) with increased values toward the surface of the comet. The increase of the primary efficiency toward the surface follows: (1) from the structure of the H_2O and CO photoabsorption and photoionization cross sections, which decrease in particular below 30 nm, giving rise to more energetic photoelectrons on average, and (2) the increased neutral densities, which causes the photoelectrons to deposit more of their energy locally.
2. The primary ions are rapidly lost through ion–neutral reactions forming H_3O^+ , which in turn, at least at low cometocentric distances, is lost rapidly by proton transfer to M_{HPA} , which were held constant at a mixing ratio of 1% in the baseline simulation.
3. The thermal electron number density peaks with a value of $\sim 8 \times 10^4 \text{ cm}^{-3} \sim 1$ km above the surface. The reason for the peak being above the surface (despite that the electron production rate is highest in the very vicinity of the surface) is related to the magnitude of the flux divergence term of the continuity equation at low cometocentric distances. For $r > 10$ km, the electron number density is approximately proportional to $1/r^{1.23}$ (see Equation (10)).
4. The ion population is dominated by $M_{\text{HPA}}\text{H}^+$ and H_3O^+ . Below about 90 km $M_{\text{HPA}}\text{H}^+$ ions start becoming more abundant than H_3O^+ , and close to the surface $M_{\text{HPA}}\text{H}^+$ account for more than 95% of the ion population.
5. Cluster ions peak in abundance near the surface with a number density of $\sim 4 \times 10^2 \text{ cm}^{-3}$.

We have conducted a series of sensitivity tests to investigate how the results of the baseline simulation are influenced by changes of input parameters: the solar EUV spectrum, the neutral number densities, the SZA, the radial speed of the ions, the cross sections for photo- and electron-impact processes, and the electron temperature profile. In particular the electron temperature strongly influences the predicted electron number densities. With T_e being set 30 K (200 K) higher than the neutral temperature, the predicted n_e increases by approximately 10% (32%) and 39% (93%) at cometocentric distances of 10 and 70 km, respectively, with respect to the results from the baseline simulation. We have also tested how the ion chemistry is influenced by the mixing ratio of M_{HPA} . Provided a negative temperature dependence for the proton transfer reaction (IN16) $\text{H}_3\text{O}^+ + M_{\text{HPA}} \rightarrow M_{\text{HPA}}\text{H}^+ + \text{H}_2\text{O}$ even a low mixing ratio of M_{HPA} (0.3%) results in a plasma dominated by ions on the form $M_{\text{HPA}}\text{H}^+$ below ~ 25 km. If the number density of M_{HPA} is increased to 5% relative to H_2O , the transition from an H_3O^+ to an $M_{\text{HPA}}\text{H}^+$ dominated plasma occurs at ~ 500 km.

Finally, we have investigated the effects on the ion chemistry of removing the temperature dependence for (1) $\text{H}_3\text{O}^+ + M_{\text{HPA}} \rightarrow M_{\text{HPA}}\text{H}^+ + \text{H}_2\text{O}$ and (2) all ion–neutral reactions. The effects are rather pronounced as demonstrated in Figures 11 and 8, respectively. To this end, we encourage further experi-

mental and theoretical efforts to determine reaction rate coefficients for ion–neutral reactions at very low temperatures (down to 10 K), in particular for reactions involving H_3O^+ as the ionic reactant.

It is stressed that we for most sensitivity tests only changed one input parameter of the baseline model. If for example the neutral densities would be four times higher than in the default simulation it would introduce a larger sensitivity to changes in, e.g., the SZA. As addressed in Section 1, the results from our model are only suitable for comparisons with measured electron and ion-number densities within the actual diamagnetic cavity of 67P/CG near perihelion where transport can be assumed radial. The boundary of this cavity has earlier been estimated at a cometocentric distance of about 30–40 km on the sunlit side of the comet (Benna & Mahaffy 2006; Hansen et al. 2007). Its location is, however, expected to be highly variable with solar conditions, outgassing level, and outward expansion velocity and may in principle be as high as hundreds of kilometers (K. Birkett & C. Carr 2012, private communication).

The potential effects of gas-dust interactions for the predictions of electron and ion number densities are beyond the scope of this paper, but will be the focus of a future study. At this stage, we cannot rule out the possibility that electron attachment to dust grains may have a significant impact on the thermal electron balance and the ion chemistry, in particular near the surface. As an example of a dusty plasma, *Cassini* observations revealed a very pronounced depletion of gas-phase electrons to dust grains in the plume of Enceladus (Morooka et al. 2011). As another interesting example from *Cassini* observations, in the deep ionosphere of Titan, below about 900 km, the negatively charged population is predominantly composed of complex macromolecular ions rather than free electrons (Ågren et al. 2012; Lavvas et al. 2013).

On the one hand, when the coma will be well developed the ion and electron number density in situ measurements from ROSINA, LAP, and MIP will be used for comparison with model output. On the other hand, the in situ ROSINA measurements of neutral number densities, temperature, and velocity, the in situ measured electron temperatures by LAP and MIP, and the solar EUV-spectra measured during the same time interval can be used to drive the model. We anticipate incorporating a more detailed chemical scheme following the establishments of volume-mixing ratios of various minor molecules versus cometocentric distance. Of particular interest are the volume-mixing ratios of the various molecules with higher proton affinity than H_2O , as these are anticipated to dictate which ions are most abundant within the diamagnetic cavity of 67P/CG near perihelion.

E.V. is grateful for funding from the Swedish Research Council (contract No. 2011-894). M.G. is partially funded by the Science & Technology Facilities Council (STFC) through the consolidating grant to Imperial College London. We thank Chris Carr at Imperial College London for introducing us to the *Rosetta* endeavor and for very inspiring and enriching discussions. We also thank John Holland, Kimberley Birkett, and Giulia Boucher for their participation and enthusiasm while building this project. We acknowledge V. M. Tenishev and M. Combi at the University of Michigan for kindly providing us the neutral input data for our model through the ICES effort (<http://www.ices.engin.umich.edu>). We thank the TIMED/SEE PI, Tom Woods, and his team for providing us with the solar flux data sets.

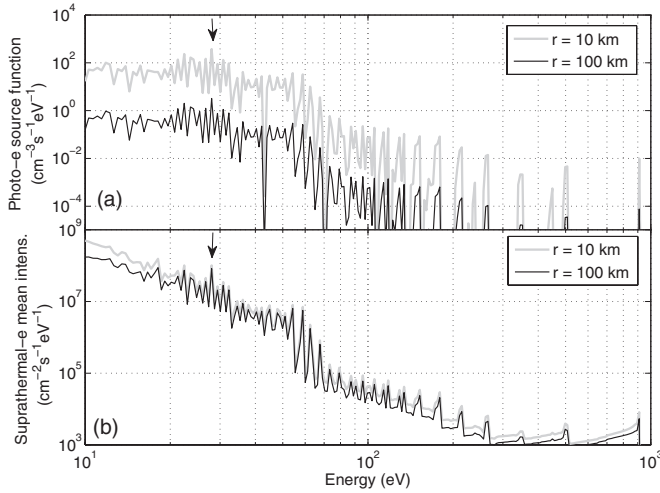


Figure 12. (a) Photoelectron source functions vs. photoelectron energy computed for the baseline simulation at cometocentric distances of 10 km (gray line) and 100 km (black line). (b) Total suprathermal electron mean intensity vs. suprathermal electron energy computed for the baseline simulation at cometocentric distances of 10 km (gray line) and 100 km (black line). The vertical arrows indicate the strongest photoelectron peak (at 28.2 eV) in the spectra associated with He II (30.4 nm) photons ionizing H₂O and producing H₂O⁺.

APPENDIX

The photoelectron source function computed at cometocentric distances of 10 km and 100 km is shown as a function of the photoelectron energy in Figure 12(a). It is derived from the attenuated solar flux calculated from the Beer–Lambert Law (see Section 2.1). A photoelectron generated by a photon of wavelength λ through the ionization of a molecule with an associated ionization potential IP has an energy given by

$$E(\text{eV}) = \frac{hc}{q \times \lambda} - \text{IP}(\text{eV}), \quad (\text{A1})$$

where h , c , and q are Planck’s constant, the speed of light, and the elementary charge, respectively. The most prominent peak in the spectra is located near 28 eV and is identified by a vertical arrow in the figure. These electrons are associated with He II solar photons (30.4 nm) ionizing H₂O and producing H₂O⁺ (IP = 12.62 eV) with the energy of the ejected photoelectron being 28.2 eV. Another prominent peak is seen near 23 eV, associated with He II solar photons causing dissociative ionization of H₂O producing OH⁺ (IP = 18.1 eV), with the energy of the ejected photoelectron being 22.7 eV. The difference between the spectra at 10 km and 100 km reflects mainly the difference in the ambient neutral densities at these cometocentric distances. It is noted that some spike features in Figure 12(a) result only from the 1 nm spectral resolution of the solar EUV spectrum and the discrete method of distributing photoelectrons into given energy bins. As a result, some photoelectron energy bins are not filled in, resulting for example in the gap in the photoelectron source function near 43.5 eV. Such gaps do not have a significant influence on the resulting electron-impact ionization rates (integrated over energy).

The suprathermal electron mean intensity is shown as a function of the electron energy at cometocentric distances of 10 km and 100 km in Figure 12(b). It represents the average over pitch angle of the suprathermal electron intensity I_e . The latter is the solution of the Boltzmann equation driven by the photoelectron source function (see Section 2.1). The suprathermal electron mean intensity includes photoelectrons,

their degradation in energy, and secondary electrons produced by electron-impact on atmospheric neutrals. The photoelectron signatures near 23 and 28 eV prominent in the photoelectron source function are still present in the suprathermal electron intensity spectra. The suprathermal electron mean intensities for $E > 80$ eV are typically about 50%–60% higher at 10 km than at 100 km (the difference is somewhat smaller for $20 \text{ eV} < E < 80 \text{ eV}$). This pronounced difference is due to transport effects, and the difference is not seen when a local approximation approach is applied, that is, the transport of suprathermal electrons is ignored (in this case the dominant terms in the Boltzmann equation are all proportional or nearly proportional to the ambient neutral density).

REFERENCES

- Adams, N. G., Smith, D., & Grief, D. 1978, *Int. J. Mass. Spectrom. Ion Phys.*, 26, 405
- Adams, N. G., Smith, D., & Paulson, J. F. 1980, *JCP*, 72, 288
- Ågren, K., Edberg, N. T., & Wahlund, J.-E. 2012, *GeoRL*, 39, L10201
- Anicich, V. G., Huntress, W. T., & Futrell, J. H. 1976, *CPL*, 40, 233
- Anzai, K., Kato, H., Hoshino, M., et al. 2012, *EPJD*, 66, 36
- Avakyan, S. V., Il’in, R. N., Lavrov, V. M., & Ogurtsov, G. N. 1998, *Collision Processes and Excitation of UV Emission from Planetary Atmospheric Gases. A Handbook of Cross Sections* (London: Gordon and Breach)
- Balsiger, H., Altwegg, K., Bochsler, P., et al. 2007, *SSRv*, 128, 745
- Benna, M., & Mahaffy, P. R. 2006, *GeoRL*, 33, L10103
- Bhardwaj, A. 2003, *GeoRL*, 30, 2244
- Bhardwaj, A., Haider, S. A., & Singhal, R. P. 1990, *Icar*, 85, 216
- Biver, N., Crovisier, J., Bockelée-Morvan, D., et al. 2012, *A&A*, 539, A68
- Bockelée-Morvan, D., Lis, D. C., Wink, J. E., et al. 2000, *A&A*, 353, 1101
- Brunger, M. J., & Buckman, S. J. 2002, *PhR*, 357, 215
- Budzien, S. A., Festou, M. C., & Feldman, P. D. 1994, *Icar*, 107, 164
- Chan, W. F., Cooper, G., & Briton, C. E. 1993a, *CP*, 178, 387
- Chan, W. F., Cooper, G., & Briton, C. E. 1993b, *CP*, 170, 123
- Chatterjee, B. K., & Johnsen, R. 1987, *JCP*, 87, 2399
- Churyumov, K. I., & Gerasimenko, S. I. 1972, in *IAU Symp. 45, The Motion, Evolution of Orbits, and Origin of Comets*, ed. G. A. Chebotarev, E. I. Kazimirchak-Polonskaia, & B. G. Marsden (Dordrecht: Reidel), 27
- Cravens, T. E. 1987, *AdSpR*, 7, 147
- Cravens, T. E. 1989, *JGR*, 94, 15025
- Cravens, T. E., & Gombosi, T. I. 2004, *AdSpR*, 33, 1968
- Cravens, T. E., & Körözmezey, A. 1986, *P&SS*, 34, 961
- Cravens, T. E., Kozyra, J. U., Nagy, A. F., Gombosi, T. I., & Kurtz, M. 1987, *JGR*, 92, 7341
- Crovisier, J. 1989, *A&A*, 213, 459
- Crovisier, J., Biver, N., Bockelée-Morvan, D., & Colom, P. 2009, *P&SS*, 57, 1162
- Davidsson, B. J. R., & Gutiérrez, P. J. 2004, *Icar*, 168, 392
- Davidsson, B. J. R., & Gutiérrez, P. J. 2005, *Icar*, 176, 453
- Davidsson, B. J. R., & Gutiérrez, P. J. 2006, *Icar*, 180, 224
- Ehrenfreund, P., & Charnley, S. B. 2000, *ARA&A*, 38, 427
- Ehrenfreund, P., Irvine, W., Becker, L., et al. 2002, *RPPH*, 65, 1427
- Eriksson, A. I., Boström, R., Gill, R., et al. 2007, *SSRv*, 128, 729
- Flammer, K. R., & Mendis, D. A. 1993, *JGR*, 98, 21003
- Galand, M., Yelle, R. V., Coates, A. J., Backes, H., & Wahlund, J.-E. 2006, *GeoRL*, 33, L21101
- Galand, M., Yelle, R., Cui, J., et al. 2010, *JGR*, 115, A07312
- Gan, L., & Cravens, T. E. 1990, *JGR*, 95, 6285
- Geppert, W. D., Hamberg, M., Thomas, R. D., et al. 2006, *FaDi*, 133, 177
- Glassmeier, K. H. 2007, *SSRv*, 128, 649
- Gombosi, T. I. 1991, *RvGeS*, 29, 976
- Häberli, R. M., Altwegg, K., Balsiger, H., & Geiss, J. 1996, *JGR*, 101, 15579
- Haider, S. A., & Bhardwaj, A. 1997, *AdSpR*, 20, 291
- Haider, S. A., & Bhardwaj, A. 2005, *Icar*, 177, 196
- Hamon, S., Speck, T., Mitchell, J. B. A., Rowe, B., & Troe, J. 2005, *JCP*, 123, 054303
- Hanner, M. S., Tedesco, E., Tokunaga, A. T., et al. 1985, *Icar*, 64, 11
- Hansen, K. C., Bagdonat, T., Motschmann, U., et al. 2007, *SSRv*, 128, 133
- Huebner, W. F., Boice, D. C., Schmidt, H. U., et al. 1989, *AdSpR*, 9, 385
- Huebner, W. F., Keady, J. J., & Lyon, S. P. 1992, *Ap&SS*, 195, 1
- Huntress, W. T., McEwan, M. J., Karpas, Z., & Anicich, V. G. 1980, *ApJS*, 44, 481
- Huntress, W. T., & Pinizzotto, R. F. 1973, *JCP*, 59, 4742

- Ip, W. H. 1985, *AdSpR*, **5**, 233
- Ip, W. H. 1989, *AdSpR*, **9**, 141
- Ip, W. H. 2004, in *Comets II, Global Solar Wind Interaction and Ionospheric Dynamics*, Vol. 745, ed. M. C. Festou, H. U. Keller, & H. A. Weaver (Tucson, AZ: Univ. Arizona Press), 605
- Itikawa, Y., & Mason, N. 2005, *JPCRD*, **34**, 1
- Jackman, C. H., Garvey, R. H., & Green, A. E. S. 1977, *JGR*, **82**, 5081
- Jones, J. D. C., Birkinshaw, K., & Twiddy, N. D. 1981, *CPL*, **77**, 484
- Karpas, Z., Anicich, V. G., & Huntress, W. T. 1978, *CPL*, **59**, 84
- Kato, H., Kawahara, H., Hoshino, M., et al. 2007, *JCP*, **126**, 064307
- Kim, J. K., & Huntress, W. T. 1975, *JCP*, **62**, 2820
- Körözmezey, A., Cravens, T. E., Gombosi, T. I., et al. 1987, *JGR*, **92**, 7331
- Królikowska, M. 2003, *AcA*, **53**, 195
- Lamy, P. I., Toth, I., Davidsson, B. J. R., et al. 2007, *SSRv*, **128**, 23
- Lavvas, P., Yelle, R. V., Koskinen, T., et al. 2013, *PNAS*, **110**, 2729
- Lovell, A. J., Kallivayalil, N., Schloerb, F. P., et al. 2004, *ApJ*, **613**, 615
- Ma, Y.-J., Altwegg, K., Breus, T., et al. 2008, *SSRv*, **139**, 311
- Mackay, G. I., Tanner, S. D., Hopkinson, A. C., & Bohme, D. K. 1979, *CaJCh*, **57**, 1518
- Mangan, M. A., Lindsay, B. G., & Stebbings, R. F. 2000, *JPhB*, **33**, 3225
- Marconi, M. L., & Mendis, D. A. 1988, *ApJ*, **330**, 513
- Masuoka, T., & Nakamura, E. 1993, *PhRvA*, **48**, 4379
- Masuoka, T., & Samson, J. A. R. 1981, *JCP*, **74**, 1093
- McLain, J. L., & Adams, N. G. 2009, *P&SS*, **57**, 1642
- Mendis, D. A. 1988, *ARA&A*, **26**, 11
- Mendis, D. A., Hill, J. R., Houppis, H. L. F., & Whipple, E. C. 1981, *ApJ*, **249**, 787
- Mitchell, J. B. A. 1990, *PhR*, **186**, 215
- Morooka, M. W., Wahlund, J.-E., Eriksson, A. I., et al. 2011, *JGR*, **116**, A12221
- Muñoz, A., Oller, J. C., Blanco, F., et al. 2007, *PhRvA*, **76**, 052707
- Néau, A., Al Khalili, A., Rosén, S., et al. 2000, *JCP*, **113**, 1762
- Neubauer, F. M., Glassmeier, K. H., Pohl, M., et al. 1986, *Natur*, **321**, 352
- Nordholt, J. E., Reisenfeld, D. B., Wiens, R. C., et al. 2003, *GeoRL*, **30**, 1465
- Ogilvie, K. W., Coplan, M. A., Bonchsler, P., & Geiss, J. 1986, *Sci*, **232**, 374
- Öjekull, J., Andersson, P. U., Na'Ga'Rd, M. B., et al. 2004, *JCP*, **120**, 7391
- Opal, C. B., Peterson, W. K., & Beaty, E. C. 1971, *JCP*, **55**, 4100
- Pätzold, M., Häusler, B., Aksnes, K., et al. 2007, *SSRv*, **128**, 599
- Plummer, E. W., Gustafsson, T., Gudat, W., & Eastman, D. E. 1977, *PhRvA*, **15**, 2339
- Poparic, G. B., Belic, D. S., & Vivic, M. D. 2006, *PhRvA*, **73**, 062713
- Rees, M. H. 1989, *Physics and Chemistry of the Upper Atmosphere* (Cambridge Atmospheric and Space Science Series; Cambridge: Cambridge Univ. Press)
- Rodgers, S. D., & Charnley, S. B. 2001, *MNRAS*, **320**, L61
- Rosén, S., Derkatch, A., Semaniak, J., et al. 2000, *FaDi*, **115**, 295
- Rosén, S., Peverall, P., Larsson, M., et al. 1998, *PhRvA*, **57**, 4462
- Rubin, M., Hansen, K. C., Gombosi, T. I., et al. 2009, *Icar*, **199**, 505
- Schmidt, H. U., Wegmann, R., & Neubauer, F. M. 1993, *JGR*, **98**, 21009
- Schulz, R. 2009, *SoSyr*, **43**, 343
- Schunk, R. W., & Nagy, A. F. 2009, *Ionospheres: Physics, Plasma Physics, and Chemistry* (Atmospheric and Space Science Series; Cambridge: Cambridge Univ. Press)
- Smith, D., & Spanel, P. 2001, *Rapid Commun. Mass Spectrom.*, **15**, 563
- Smith, D., Spanel, P., & Mayhew, C. A. 1992, *IJMSI*, **117**, 457
- Tenishev, V., Combi, M., & Davidsson, B. 2008, *ApJ*, **685**, 659
- Thorn, P. A. 2008, PhD thesis, Flinders Univ. South Australia
- Tian, C., & Vidal, C. R. 1999, *PhRvA*, **59**, 1955
- Trotignon, J. G., Michau, J. L., Lagoutte, D., et al. 2007, *SSRv*, **128**, 713
- von Oertzen, J. 2003, PhD thesis, Univ. Cologne
- Wegmann, R., Schmidt, H. U., & Bonev, T. 1996, *A&A*, **306**, 638
- Wegmann, R., Schmidt, H. U., Huebner, W. F., & Boice, D. C. 1987, *A&A*, **187**, 339
- Woodall, J., Agúndez, M., Markwick-Kemper, A. J., & Millar, T. J. 2007, *A&A*, **466**, 1197
- Woods, T. N., & Eparvier, F. G. 2006, *AdSpR*, **37**, 219
- Woods, T. N., Eparvier, F. G., Bailey, S. M., et al. 2005, *JGR*, **110**, A01312
- Zolensky, M. E., Zega, T. J., Yano, H., et al. 2006, *Sci*, **314**, 1735